2019

Chemical Properties, Structural Properties, and Energy Storage Applications of Prussian Blue Analogues

Weijie Li
University of Wollongong, weijie@uow.edu.au

Chao Han
University of Wollongong, chan@uow.edu.au

Gang Cheng
Wuhan Institute of Technology

Shulei Chou
University of Wollongong, shulei@uow.edu.au

Hua-Kun Liu
University of Wollongong, hua@uow.edu.au

See next page for additional authors

Publication Details

Li, W., Han, C., Cheng, G., Chou, S., Liu, H. & Dou, S. (2019). Chemical Properties, Structural Properties, and Energy Storage Applications of Prussian Blue Analogues. Small, 15 (32), 1900470-1-1900470-21.

Chemical Properties, Structural Properties, and Energy Storage Applications of Prussian Blue Analogues

Abstract
Prussian blue analogues (PBAs, A 2 T[M(CN) 6], A = Li, K, Na; T = Fe, Co, Ni, Mn, Cu, etc.; M = Fe, Mn, Co, etc.) are a large family of materials with an open framework structure. In recent years, they have been intensively investigated as active materials in the field of energy conversion and storage, such as for alkaline-ion batteries (lithium-ion, LIBs; sodium-ion, NIB; and potassium-ion, KIBs), and as electrochemical catalysts. Nevertheless, few review papers have focused on the intrinsic chemical and structural properties of Prussian blue (PB) and its analogues. In this Review, a comprehensive insight into the PBAs in terms of their structural and chemical properties, and the effects of these properties on their materials synthesis and corresponding performance is provided.

Disciplines
Engineering | Physical Sciences and Mathematics

Publication Details
Li, W., Han, C., Cheng, G., Chou, S., Liu, H. & Dou, S. (2019). Chemical Properties, Structural Properties, and Energy Storage Applications of Prussian Blue Analogues. Small, 15 (32), 1900470-1-1900470-21.

Authors
Weijie Li, Chao Han, Gang Cheng, Shulei Chou, Hua-Kun Liu, and Shi Xue Dou

WILEY-VCH

DOI: 10.1002/ ((please add manuscript number))
Article type: ((**Review**))

Chemical properties, structural properties, and energy storage applications of Prussian blue analogues

*Wei-Jie Li,[a,] *Chao Han,[a] Gang Cheng,[b] Shu-Lei Chou,[a,] * Hua-Kun Liu,[a] Shi-Xue Dou[a]*

[a]Dr. W. J. Li, Dr. C. Han, Prof. S. L. Chou, Prof. H.K. Liu, Prof. S. X. Dou
Institute for Superconducting and Electronic Materials, University of Wollongong.
Wollongong, NSW 2522 Australia
[b]Dr. G. Cheng
School of Chemistry and Environmental Engineering, Wuhan Institute of Technology,
Xiongchu Avenue, Wuhan 430073, PR China
E-mail: wl347@uowmail.edu.au; shulei@uow.edu.au

Keywords: Prussian blue analogues, Chemical property, Structural property, Influence of properties on applications

Prussian blue analogues (PBAs, $A_2T[M(CN)_6]$, A= Li, K, Na; T=Fe, Co, Ni, Mn, Cu, etc.; M= Fe, Mn, Co, etc.) are a large family of materials with an open framework structure. In recent years, they have been intensively investigated as active materials in the field of energy conversion and storage, such as alkaline ion batteries (lithium ion: LIBs, sodium ion: NIBs, and potassium ion: KIBs), and as electrochemical catalysts. Nevertheless, few reviews papers have focused on the intrinsic chemical and structural properties of Prussian blue (PB) and its analogues. In this review, the authors aim to provide comprehensive insight into the Prussian blue analogues in terms of structural and chemical properties, and the effects of these properties on materials synthesis and the corresponding performance.)

1. Introduction

Global warming and fossil fuel depletion has become an increasing concern in recent decades, impelling researchers to pay more attention to the utilization of green power sources. The utilization of solar power, wind power, and hydrogen energy not only requires the energy conversion devices, such as solar cells, water splitting devices, etc., but also needs energy storage devices (alkaline ion batteries (Li, Na, K), metal-air batteries, etc.) owing to the

intermittent nature of these sources. Correspondingly, various kinds of energy conversion and energy storage materials have received intensive investigation.

Currently, phosphates (A_xTPO_4, A: alkaline ions; T: transition metal: Fe, Co, Ni, Mn, Zn, Cu, Mg, etc.), Prussian blue analogues, and transition metal oxides, carbides, nitrides, phosphides, sulphides, carbon, fluoride and pure metal materials have been introduced into the fields of energy conversion and storage.[1-17] Prussian blue analogues stand out from the other various materials (metal oxides, metal phosphides, metal sulphides, etc.), due to their facile synthesis method, low-cost raw precursors and rich redox couples which contributes to the excellent electrochemical performance.[5] Prussian blue was the first synthetic dye, prepared by mixing some cochineal (a natural red dye) with iron sulfate and a cyanide mixture in 1704. In fact, Prussian blue is ferric ferrocyanide ($Fe_4^{3+}[Fe^{2+}(CN)_6]_3$) which is a coordination material. Prussian blue can be synthesized chemically by mixing ferric (ferrous) and hexacyanoferrate ions with different oxidation states of the iron atoms: either Fe^{3+} + $[Fe^{2+}(CN)_6]^{4-}$ or Fe^{2+}+ $[Fe^{3+}(CN)_6]^{3-}$.[18] Afterwards, a variety of Prussian blue analogues (PBAs) with the chemical formula $A_xT[M(CN)_6].n\ H_2O$ are developed, where A represents an alkaline ion (Li, Na, K), T represents an early transition metal (T = Fe, Co, Ni, Mn, Zn, Cu, Mg, etc.), and M represents the transition metal (M = Mn, Fe, Co). Owing to its open framework, the alkaline ions can be extracted/intercalated reversibly into the PBAs, making them suitable as cathode materials for alkaline ion batteries (Li^+, Na^+, K^+, etc.) and as electrodes for supercapacitors with organic or aqueous electrolytes.[19-63] Some defects and crystal water inevitably remain in PBAs due to its preparation in aqueous solution, meaning that it can be used as the host for hydrogen storage.[64-66] In addition, due to the abundant transition metal in the framework, PBAs and their derivatives can be applied as catalysts for the oxygen evolution reaction (OER) and hydrogen evolution reaction (HER). [67-75]

A few reviews have been published on PBAs recently, mainly focusing on the synthesis of Prussian blue and its application on sodium ion batteries. In terms of their intrinsic structural and chemical properties and other applications, however, to the best of our knowledge, there is no review that comprehensively summarizes them, especially relating to the corresponding effects in applications of PBAs. Therefore, in this review, the authors aim to provide a comprehensive overview of the latest research progress on the Prussian blue analogues. First, the synthesis methods and the structural and chemical properties of PBAs are discussed. Secondly, a variety of applications for these PBAs are introduced, such as alkaline ion batteries, hydrogen storage, morphology templates, and catalysis. Then, the effects of their structural and chemical properties on materials synthesis and their performance in corresponding applications are discussed. Finally, some personal viewpoints on the challenges and outlook for PBAs application are included.

2. Synthesis approaches

Generally, the synthesis methods for PBAs are classified into three main kinds: 1) the precipitation method; 2) the hydrothermal method, and 3) the electrodeposition method, as shown in **Figure 1**. The features and details of each synthesis approach will be discussed as follows.

2.1 Precipitation method

Various PBAs have been prepared by the precipitation method, in which a solution of the metal-ion salts is mixed with a solution of ferrocyanide ligands to produce the PBAs.[21-23, 26-27, 29, 32, 35-37, 39, 41, 56, 68, 76-78] The obtained PBAs present a random morphology owing to the fast reaction between the ligands and the metal ions, as shown in Figure 2a.[41, 76] To control the morphology of PBAs prepared by the precipitation method, coordination agents are utilized to slow the reaction rates. Consequently, two-dimensional (2D) $Ni[Ni(CN)_4]$ nanoflakes are

obtained via introducing trisodium citrate dehydrate as the coordination agent (Figure 2b).[69] Three-dimensional (3D) $Na_2CoFe(CN)_6$ nanocubes, as shown in Figure 2c, are also synthesized by using trisodium citrate as the chelating agent.[44] $K_xMn[Fe(CN)_6]$ nanocubes are also prepared by the precipitation method with sodium citrate as the chelating agent.[50] Conducting polypyrole (PPy) in a composite with $Na_{1.72}MnFe(CN)_6$ is prepared by the precipitation method.[63] PPy serves not only as a conductive coating layer to improve the rate capability, but also as a protective layer to reduce the dissolution of Mn into the electrolyte to improve the cycling performance.

Based on the precipitation, some acid/photon – assisted precipitation synthesis approaches are developed to prepare various PBAs, where the metal ions are indirectly provided with the assistance of acid or photon. Zhang X. group reported the acid-assisted precipitation synthesis method to prepare PB@stainless-steel meshes (PB@SSM). At first, the metal (Fe, Ni, Cr) oxide/hydroxide was prepared through immersing stainless-steel meshes into aqueous ammonia solution under hydrothermal condition. Then, the metal oxide/hydroxide is immersed into a potassium ferrocyanide solution containing dilute hydrochloride acid. In this progress, the metal oxide/hydroxide will be dissolved into Fe, Ni, Cr ions with the acid assistance, which are immediately precipitated with ferricyanide ions to form PBAs.[13] A flexible electrodes of Prussian Blue (PB) on Xuan paper are synthesised by using photosensitizer solution as the precursor.[12] The photosensitizer solution is obtained by mixing the aqueous solution of ferric ammonium citrate and the solution of $K_3Fe(CN)_6$. The Fe^{3+} ions in Photo-sensitizer solution (ferric ammonium citrate) is reduced to Fe^{2+} ions under UV light, and then the generated Fe^{2+} ions are immediately precipitated with excess ferricyanide ions to form the PB on the Xuan paper. Notably, due to the insufficient supply of Fe2+ ions, the rate of crystal nucleation and growth of PB is retained, thus resulting in improving crystallinity and dispersion of PB particles.

2.2 Hydrothermal method

The hydrothermal method is a popular method to prepare Prussian blue microparticles, where the decomposition of $Fe(CN)_6^{4-}$ into Fe^{3+}/Fe^{2+} in acid solution is utilized to react with the residual $Fe(CN)_6$ to form PB.[8, 33, 79] $Co_3[Co(CN)_6]_2$ PBA is also prepared under acid-assisted hydrothermal conditions.[80] $Co_3[Co(CN)_6]_2$ PBAs with various nanostructures (nanocubes and nanorods) are prepared under non-acid solvothermal conditions with $K_3[Co(CN)_6]$ as the single-source precursor. The $K_3[Co(CN)_6]$ partially dissociates into Co^{3+}/Co^{2+} ions in water droplets at higher temperature, and then reacts with un-dissociated $[Co(CN)_6]^{3-}$ ions to form $Co_3[Co(CN)_6]_2$.[81] It should be noted that the ferricyanide complex ($Fe(CN)_6^{4-}$, $Co(CN)_6^{4-}$) is the single precursor in these synthesis processes. Thus, this method is suitable to form PBAs containing a single transition metal ($A_xT[M(CN)_6]\cdot nH_2O$ (T=M, Co, Fe, etc.)).[81] During the hydrothermal/solvethermal process, through modulating the surfactant and the molar ratio of H_2O to surfactant, various morphology of PBAs can be obtained (Figure 3), including nanocubes ($A_xFe[Fe(CN)_6].nH_2O$ (A = K, Na) and $Co_3[Co(CN)_6]_2$),[14, 33, 51, 59, 81] nanorods ($Co_3[Co(CN)_6]_2$)[81], and nanopolyhedra ($Co_3[Co(CN)_6]_2$)[81]. Liu Y. et al. found that the acid not only triggered the chemical reaction but also acted as an etching reagent to tailor the morphology.[51] As shown in Figure 3d, when the added amount of HCl is 1 mL, PB microcubes are obtained. Then, the surface of the PB cubes with concave centres became very rough with 2 mL HCl addition (Figure 3e, h). Finally, porous PB spheres are obtained when 3 mL HCl is added into the system (Figure 3 f, i). Based on the hydrothermal method, a variety of PB-carbon composites have been synthesized, including PB – reduced graphene oxide composite (PB/rGO), [52, 59] PB - carbon nanotube (PB/CNT) composite, [45] and PB - polypore (PB/PPy)) composite.[42] $Na_xFe[Fe(CN)_6]$ PB-graphene and PB/PPy composites are prepared by a two-step method where PB particles are first synthesized by the hydrothermal method, and then rGO or PPy are coated on the surfaces of PB particles (Figure 4 a- d).[42, 52] Our group reported a facile one-step hydrothermal method to prepare PB/rGO composite

utilizing the decomposition product of Fe^{2+} to reduce graphene oxide (GO) (Figure 4 (j)).[59] PB/CNT composite was synthesized by a one-step hydrothermal method acting on $Na_4Fe(CN)_6$ and CNT in acid solution (Figure 4 e-h)).[45]

2.3 Electrodeposition method

N. Vernon was the first to propose that Prussian blue could be deposited directly by electrochemical reaction from an Fe^{3+} and $[Fe(CN)_6]^{4-}$ acidic solution.[82] Afterwards, $Fe_4[Fe(CN)_6]_3.xH_2O$ nanowires were electrodeposited on a polycarbonate membrane via chronoamperometry under the potential of 0.3 V (vs. saturated calomel electrode (SCE)) by immersing the working electrode in a fresh solution containing $FeCl_3$, $K_3Fe(CN)_6$, H_3BO_4, and KCl. [83-84] $Fe_4[Fe(CN)_6]_3.xH_2O$ nanotubes were prepared by electrodeposition on anodized porous aluminium foil. Some PB particles were initially deposited on the membrane, and then these particles became large enough to form a complete film coating the walls of the anodic alumina pores after several deposition cycles. PB nanotubes were obtained after selective etching of the alumina template (Figure 5b). [85] Due to the low solubility of ferrocyanide salts in organic solution, the PBAs are primarily prepared in aqueous solution. Consequently, the obtained PBAs inevitably contain crystal or coordination water in the framework and defects, which will be further discussed in detail.

3. Structural properties

3.1 Cubic /monoclinic/rhombohedral structure

The formula for PBAs is $A_xT[M(CN)_6].n\ H_2O$ (A = Li, Na, K; T/M = Fe, Co, Ni, Mn, Zn, Cu, Mg, etc.). Usually, the transition metal coordinated with N presents the high-spin state and the one coordinated with C presents the low-spin state. PBAs have 3 kinds of polymorphs: monoclinic, cubic, and rhombohedral phases, as shown in Figure 6. The PBA structure is influenced by the number of alkaline ions and amount of zeolitic water in the framework. Kojima et al. reported that the $A_xMn[Mn(CN)_6].nH_2O$ structure depended on the amount of

alkaline ions in the framework. When the alkaline ion concentration is low ($x < 1$), the unit cell presents the cubic phase. With a high alkaline ion concentration of $x = 1.72$, $A_{1.72}Mn[Mn(CN)_6].nH_2O$ exhibits the monoclinic phase. When the alkaline ion concentration is in the range of $1 < x < 1.72$, a two-phase process between the cubic and monoclinic phases exists (Figure 7a). [25] In the case of $Na_xMn[Fe(CN)_6]$, $Na_{1.72}Mn[Fe(CN)_6]$ and $Na_{1.40}Mn[Fe(CN)_6]$ exhibited monoclinic and cubic phases, respectively.[29, 63] Therefore, it is concluded that the alkaline-deficient PBAs presents the cubic phase, while alkaline-rich PBAs usually present the monoclinic phase.

In addition to the influence of the alkaline ion concentration, the amount of zeolitic water in the framework also affects the unit cell structure. Goodenough's group reported rhombohedral $Na_{2-\delta}MnFe(CN)_6$ that was obtained through dehydrating monoclinic $Na_{2-\delta}MnFe(CN)_6$ at 100° C for 30 h under a 15 m Torr vacuum.[36-37] Figure 8(a, c) shows the synchrotron X-ray diffraction (SXRD) patterns of the monoclinic and rhombohedral $Na_{2-\delta}MnFe(CN)_6$, respectively. The refinement results show the details of the monoclinic and rhombohedral $Na_{2-\delta}MnFe(CN)_6$ belonging to space group = P21/n (a = 10.5864, b = 7.5325, c = 7.3406 Å, and β = 92.119°) and space group = $R\bar{3}$ ($a = b$ = 6.5800 Å, c = 18.9293 Å), respectively.[36] It should be noted that monoclinic and rhombohedral $Na_{2-\delta}MnFe(CN)_6$ have the same composition except for the water content, demonstrating that the zeolitic water plays a key role in the structure of $Na_{2-\delta}MnFe(CN)_6$.

3.2 Zeolitic / Coordinated water

As they are prepared in aqueous solution, PBAs inevitably absorb water on their surfaces or in the framework. The water exists in 3 kinds of forms in the PBA framework: 1) absorbed water on the surface of PBAs; 2) the zeolitic water located in the interstitial sites, and 3) the coordinated water, which is chemically coordinated with the M ions. Figure 9(a) shows a typical face-centred cubic (fcc) crystal structure for PBAs. There are eight subunit cells in

each PBA unit cell, which can accommodate not only alkaline ions, but also neutral molecules (H_2O). Therefore, zeolitic water is the water occupying the octahedral centres of the subunits, denoted by 1 in Figure 9(a). In the PBA framework, the other water form is coordinated water, which is chemically bonded with the unsaturated metal ions because of the $M(CN)_6$ vacancies that exist at the centres of the unit cells. The absorbed and zeolitic water is easy to remove because the water is just physically adsorbed on the surface or in the interstitial lattice sites. In contrast, the coordinated water is difficult to remove from the PBAs due to its bonding with metal ions.[20]

The amount of water in PBA frameworks can be characterized quantitatively by thermogravimetric analysis (TGA). The weight loss occurring below 200 °C corresponds to the physically absorbed and zeolitic water, and the sequential weight loss at the temperature range of 200-300 °C is associated with the coordinated water (Figure 9(b)). The higher temperature is required because the coordinated water bonds with the $M(CN)_6$ vacancies in PBA framework. Therefore, it was reported that the amount of $M(CN)_6$ vacancies can be detected through measuring the amount of coordinated water via TGA.[86]

It was reported that the particle size has an effect on the adsorption of water, that is, smaller crystals may cause a stronger adsorption of water.[69] Our group proposed one approach to reduce the water content of $Na_xFeFe(CN)_6$ through introducing more Na ions into the octahedral centres of the subunits.[8] The amount of water in the $Na_{2-\delta}$MnHCF structure can be reduced through dehydrating it at a high temperature under high vacuum conditions.[36-37] Yang et al. reported that the amount of water in the PB framework can be reduced by suppressing lattice defects. Defect-rich PB had the formula of $Fe[Fe(CN)_6]_{0.71}\cdot\square_{0.29}\cdot 4.6H_2O$ ($\square$ represents the $Fe(CN)_6$ vacancies), while low-defect PB showed the formula of $Fe[Fe(CN)_6]_{0.87}\cdot\square_{0.13}\cdot 3.1H_2O$.[43-44] Therefore, some strategies to reduce the amount of water

in PBAs include: 1) coarsening the PBA particles to reduce the adsorption on the surface; 2) dehydrating PBA samples at higher temperature under high vacuum conditions; 3) introducing more alkaline ions into the framework to reduce the adsorption sites of zeolitic water; and 4) reducing the amount of $M(CN)_6$ vacancies to decrease the coordinated sites of coordinated water.

3.3 Defects/Vacancies

It was reported that, during the conventional rapid precipitation process, large amounts of $M(CN)_6$ vacancies occupied by coordinated water will exist in the crystal framework, leading to an actual chemical formula of $A_xT[M(CN)_6]_{1-y}\cdot\square_y\cdot nH_2O$ ($0 < x < 2$; $0 < y < 1$) in which the $\square$ symbol represents the $M(CN)_6$ vacancies.[26] The appearance of $M(CN)_6$ vacancies will have some influence on the PBA structure. At first, some coordinated water will exist and coordinate with metal ions in the PBA framework, as shown in Figure 10(b). Secondly, the amount of alkaline ions in the PBA unit cell will be reduced according to the law of charge balance. Thirdly, the $M(CN)_6$ vacancies will be distributed randomly in the PBA framework, resulting in structural instability due to the vulnerability to collapse.

Low-defect $FeFe(CN)_6$ nanocrystals were obtained by slowing down the reaction rate via the acid-assisted hydrothermal method. The single precursor $K_3Fe(CN)_6$ slowly decomposes into Fe^{3+}/Fe^{2+} in the acid solution, and then reacts with the residual $Fe(CN)_6^-$, forming low-defect $FeFe(CN)_6$ nanocrystals.[33, 43] Highly crystallized $Na_2CoFe(CN)_6$ with suppressed lattice defects is obtained via the precipitation method with the assistance of sodium citrate as the chelating agent.[44] High-quality $Na_xFeFe(CN)_6$ was prepared by raising the amount of sodium in the framework through increasing the sodium ion concentration in the reaction solution.[8, 30, 33] In summary, the strategies for reducing vacancies in PBA frameworks can include: 1) reducing the rate of chemical reaction; 2) utilization of a chelating agent that can coordinate

with metal ions to slow down the reaction rate; and 3) raising the alkaline ion concentration in the unit cell of the PBA through introducing more alkaline ions into the reaction solution.

4. Chemical properties

4.1 Chemical etching under acid/alkaline solution

PBAs can be chemically etched under acid/alkaline solution, which is utilized to synthesize various hollow PBA structures.[87-93] Yamauchi et al. reported that hollow Prussian blue (PB) particles can be prepared by etching PB mesocrystals in HCl solution in the presence of polyvinylpyrrolidone (PVP). Figure 11 shows the formation mechanism in details. The interior cavity appeared in the centres of the PB mesocrystals after etching for 3.5 h. The cavity became larger on extending the etching time to 4 h (Figure 11(c)). PB nanocrystals were totally dissolved after etching for 5 h. It should be noted that PVP plays an important role in decreasing the etching rate on the particle surface to obtain hollow PB particles.[89]

David Lou et al. reported that $Fe(OH)_3$ microboxes can be obtained through the reaction between PB microcubes and NaOH solution, as shown in Equation (1),

$$12OH^- + Fe[Fe(CN)_6]_3 \rightarrow 3Fe(CN)_6^{4-} + 4Fe(OH)_3 \quad (1).$$

Actually, this reaction is an ion exchange reaction which takes place at the interface between the solid PB microcubes and the liquid alkaline solution, leading to the formation of a thin layer of $Fe(OH)_3$ on the PB surface. [87] If the reaction proceeds at room temperature, the whole PB microcube is gradually consumed, accompanied by the growth of the $Fe(OH)_3$ shell, and eventually evolving into well-defined $Fe(OH)_3$ microboxes with large interior cavities. If the inward diffusion of OH^- is accelerated by raising the temperature, yolk-shell or multishelled structures are obtained. Not only can a strong base react with PB, but also, the conjugate base of a metal/metalloid oxide ($K_2SnO_3 \cdot 3H_2O$, Na_2GeO_3, etc.) can react with PB due to the partial hydrolysis. Taking K_2SnO_3 as an example, the reaction proceeds by the following Equation (2):

$6SnO_3^{2-} + Fe_4[Fe(CN)_6]_3 + 6(1+_x)H_2O \rightarrow 3Fe(CN)_6^{4-} + 6SnO_2\ xH_2O + 4Fe(OH)_3$ (2).

After the heat-treatment, composite hollow metal oxide microboxes, composed of Fe_2O_3/SnO_2, are obtained (Figure 12). Based on this property, PB can be used as template to synthesize hollow microboxes from single shell to multishell forms with hierarchical architectures and composite hollow microboxes.

Ni-Co PBA nanocages were obtained through etching PBA cubes with ammonia at room temperature for several hours.[88] The morphology evolution was investigated by time-dependent experiments. The eight corners of each cube are first etched by ammonia due to their higher surface energy compared with flat planes, as shown in Figure 13 (b, f). As the etching time is extended, the etching process preferentially proceeds along the diagonal of the cubes (Figure 13c, g). Ho et al. reported that CoFe-PBA nanoframes can be etched by thioacetamide (TAA) relies on alkaline etching. TAA can generate ammonium under aqueous conditions by reduction of hexacyanoferrate compound. The ammonium successively breaks the coordination bonds to generate Co^{2+} and $Fe(CN)_6^{4-}$, forms complexes with Co^{2+}, and prevents the further formation of cobalt compounds on the structure. [94]

4.2 Cation Exchange

The cations in PBAs can be exchanged with other metal ions, M^{n+} (M = Co, Ni), which is utilized as a template to prepare hollow inorganic nanoparticles.[95-96] This approach takes advantage of the higher solubility of Mn-Fe PBA than other members of the PBA family, e.g., Co-Fe PBA. At the beginning of the cation exchange, Mn-Fe PBA cubes dissociate in water, leading to the establishment of a solid/liquid equilibrium, i.e., $Mn_3[Fe(CN)_6]_2 \leftrightarrow 3Mn^{2+} + 2[Fe[CN]_6]^{3-}$. When Co^{2+} or Ni^{2+} ions are introduced into the mixed solution above, the $[Fe[CN]_6]^{3-}$ ions react with Co^{2+} or Ni^{2+} ions to form Co-Fe PBA or a Ni-Fe PBA shell on the surface of Mn-Fe PBA, obtaining the yolk@shell intermediate (Figure 14(b, e)). The further

consumption of disassociated $[Fe[CN]_6]^{3-}$ ions results in the formation of hollow Co-Fe or Ni-Fe PBA nanoboxes (Figure 14(c, f)). [96]

4.3 Anion Exchange

Not only cations (M^{2+}) in PBAs can be exchanged, but anions $[Fe(CN)_6]^{3-}$ in PBAs can also be exchanged with S^{2-} or Se^{2-}. [97-98] NiS nanoframes were prepared through the reaction between Ni-Co PBA and Na_2S. Figure 15(a) shows a schematic illustration of the formation process of NiS nanoframes.[98] At the initial stage of the exchange reaction, the edges of the nanocubes are partially etched (Figure 15(c)), because the edges of nanocubes with high curvature and probably more defects are more reactive than a smooth plane surface. When the reaction proceeds, the unique NiS nanostructures are obtained (Figure 15(e)). $CoSe_2$ and Cu-doped $CoCuSe_2$ microboxes were synthesized through an anion-exchange reaction between Co-Co PBA and Se^{2-} ions. [97] When an appropriate amount of Se^{2-} anions were exchanged with $[Co(CN)_6]^{3-}$ at elevated temperature, the solid microcubes were converted into hierarchical $CoSe_2$ microboxes (Figure 15(f-h)). Afterward, the hierarchical $CoSe_2$ microboxes were doped with Cu^{2+} ions through a subsequent cation-exchange reaction with Cu^{2+} ions (Figure 15(i-n)). Based on the anion-exchange or cation-exchange, PBAs can be used as the templates to prepare various metal sulphides and metal selenides.

4.4 Electrochemical properties

In the PBAs framework ($A_xT[M(CN)_6]_{1-y}\cdot\square_y\cdot nH_2O$ ($0 < x < 2$; $0 < y < 1$)), the two transition metals present different spin state: M coordinated with N of cyanide ligands presents high-spin state, while the T coordinated with C of cyanide ligands exhibits the low-spin state. In terms of the alkaline ion storage, both transition metal T and M are electrochemically active, and thus PBAs can theoretically accommodate two alkaline ion insertions per formula. Even though there is one kind of transition metal in the framework, such as $A_xFeFe(CN)_6$ (T=M=Fe), it also delivers two potential plateaus corresponding to two active redox during the charge-discharge process. This is because the spin state of transition metal determines the potential plateau. Our group reported $Na_xFeFe(CN)_6$ presents two pairs of peaks in the dQ/dV curve of 2.98/2.92 V and 3.74/3.42 V, which are attributed to the high-spin Fe^{2+}/Fe^{3+} couple coordinated with N of cyanide ligands and the low-spin Fe^{2+}/Fe^{3+} couple bonding to the C atoms of cyanide ligands, respectively.[8]

5. Applications

5.1 Alkaline ion ($Li^+/Na^+/K^+$) batteries

PBAs can be utilized as cathode and anode materials for alkaline ion storage ($Li^+/Na^+/K^+$), due to their open frameworks, which offer large spaces for alkaline ion insertion and extraction.[58, 60-61, 99-102] The mechanism for the use PBAs for alkaline ion storage can be expressed by Equation (3),

$$A_xT[M(CN)_6] \leftrightarrow xA^+ + T[M(CN)_6]^{x-} \quad (3).$$

Figure 16 displays the charge-discharge curves of PBAs applied as cathode/anode in non-aqueous/aqueous electrolyte for alkaline ion storage. The electrochemical performances of the representative PBAs materials are listed in Table 1.

$FeFe(CN)_6$ was tested as a cathode material for Li-ion batteries, delivering a charge capacity of 95 mAh g^{-1}.[103] The charge-discharge curves showed that the main redox peak at 2.8/3.1 V corresponds to reduction/oxidation of low-spin Fe^{2+}/Fe^{3+} ions coordinated with the carbon, and a small redox peak at 3.8/3.9 V was assigned to the reduction/oxidation of the high-spin Fe^{2+}/Fe^{3+} bonded to nitrogen (Figure 16(a)). A series of PBAs ($KMFe(CN)_6$, M = Fe, Mn, Ni, Cu, Co, Zn) were initially reported as cathode materials for sodium ion storage by Goodenough's group.[29] Afterwards, You et al. developed a high-quality $Na_{0.61}Fe[Fe(CN)_6]_{0.94}\cdot\square_{0.06}$ as cathode for sodium-ion storage with high capacity of 170 mAh g^{-1}.[33] It shows similar charge-discharge curves to that of its counterpart in lithium-ion batteries with a potential plateau of ~ 3.0 V (Figure 16(b)). Recently, $K_{0.22}Fe[Fe(CN)_6]_{0.805}\cdot\square_{0.195}\cdot 4.01H_2O$ was applied as cathode in K-ion batteries.[86] Its electrochemical performance is different from those of its counterparts in lithium-ion batteries and sodium ion batterits. Its delivered capacity was ~75 mAh g^{-1}, smaller than those for lithium/sodium-ion storage. Moreover, the potential plateau is ~3.2 V, higher than for those counterparts (Figure 16(c)).

Apart from application as cathode materials in organic electrolyte, PBAs can also be applied as cathode material in aqueous electrolyte. Cui and co-authors reported the electrochemical performance of $KCuFe(CN)_6$ for potassium ion storage in 1 M KNO_3 aqueous electrolyte.[22]

It showed a potential of ~ 0.95 V for potassium intercalation, as shown in Figure 16(d). In addition, PBAs also can be utilized as anode materials for lithium ion/potassium ion storage. Guo et al. reported $Co_3[Co(CN)_6]_2$ as an anode material for potassium ion storage, exhibiting a highly reversible capacity of 324.5 mAh g^{-1}, as shown in Figure 16(e).[104]

$Co_3[Co(CN)_6]_2$ was tested as anode for lithium ion batteries (LIBs) and showed a voltage plateau at ~ 1.5 V in the initial discharge profile, which shifted to ~ 1.0 V in subsequent cycles.[105] It delivered a high reversible capacity of 304 mAh g^{-1} for Li-ion storage (Figure 16 (f)). The electrochemical performance of PBAs in alkaline ion storage can be improved by coating conductive carbon on the surface, in such forms as carbon nanotubes (CNTs), PPy, and reduced graphene oxide (rGO). Our group reported that the $Na_{1.72}MnFe(CN)_6$@ ClO_4^--PPy showed better cycling stability than the un-coated form, because the dissolution of Mn^{2+} was alleviated.[63] Moreover, the tailoring of composites also can improve the electrochemical performance of PBAs. Ni-doped $MnFe[(CN)_6]$ shows better cyclability than that of its un-doped counterpart, because the lattice distortion caused by redox reactions of $Mn^{2+/3+}$ can be buffered by redox-inactive Ni doping.[32]

5.2 Multivalent ion (Zn^{2+}/Mg^{2+}/Ca^{2+}/Ba^{2+}/Al^{3+}) batteries

PBA compounds are also considered as a promising cathode candidates for reversible insertion/extraction of multivalent cations (Mg^{2+}, Zn^{2+}, Ca^{2+}, Ba^{2+}, and Al^{3+}), due to their open framework and large ionic channels. Figure 17 displays the charge-discharge curves of PBAs applied as cathode for multivalent-ion storage. The electrochemical performances of the representative PBAs materials are listed in Table 2.

When the multivalent ions intercalate into the PBA open framework, they will occupy the A sites in each subcell of the unit cell, as shown in Figure 17(a). Cui's group reported that $KNiFe(CN)_6$ can be applied as the host for Mg^{2+}, Ca^{2+}, and Ba^{2+} ion storage. Figure 17(b) and (c) shows the charge-discharge curves of $KNiFe(CN)_6$ in Ca^{2+} and Ba^{2+} electrolyte, respectively. During the discharge process, Ca^{2+}, and Ba^{2+} ions enter into the structure to form

$KM_xNi[Fe^{2+}(CN)_6]_{2x}[Fe^{3+}(CN)_6]_{1-2x}$.[106] $K_{0.86}Ni[Fe(CN)_6]_{0.954}(H_2O)_{0.766}$ was reported as cathode host for Zn^{2+} storage, showing a potential plateau at 1.3 V vs. Zn^{2+}/Zn (Figure 17(d)). The mechanism of Zn^{2+} storage is expressed by Equation (4):

$$K_{0.86}Ni[Fe(CN)_6]_{0.954}(H_2O)_{0.766} + xZn^{2+} \leftrightarrow K_{0.86}Zn_xNi[Fe(CN)_6]_{0.954}(H_2O)_{0.766} \quad (4).$$

One PBA compound, $K_{0.1}Cu[Fe(CN)_6]_{0.7}\cdot 3.6H_2O$, was reported as cathode for Mg^{2+} batteries in aqueous electrolyte.[107] Its charge-discharge curves for Mg^{2+} intercalation/extraction is shown in Figure 17(e). The main electrochemical reaction of $K_{0.1}Cu[Fe(CN)_6]_{0.7}\cdot 3.6H_2O$ is also the reduction/oxidation of Fe in the $Fe(CN)_6$ groups. In addition, part of the Cu is proposed to take part in the reduction/oxidation reaction by Mg^{2+} intercalation/deintercalation. Gao and co-authors reported that $KCuFe(CN)_6\cdot 8H_2O$ in aqueous electrolyte can be used for the storage of Al^{3+} ions, in accordance with two-step reactions for Al^{3+} insertion/extraction (Figure 17(f)).[108] Hydrated Al^{3+} is inserted into the $KCuFe(CN)_6\cdot 8H_2O$ framework, and therefore, different salt anions could affect the state of the hydrated Al^{3+} ions in the aqueous solution, leading to shifting of the anodic/cathodic peaks in $AlCl_3$, $Al_2(SO_4)_3$, and $Al(NO_3)_3$ solutions. Moreover, the theoretical capacity of this PBA electrode is estimated to be 58.9 mAh g^{-1}, based on the molecular formula of $KCuFe(CN)_6\cdot 8H_2O$ and the redox couple of Fe^{3+}/Fe^{2+}.

It is concluded that the specific capacity of multivalent ions (Mg^{2+}, Zn^{2+}, Ca^{2+}, Ba^{2+}, and Al^{3+}) greatly depends on the M^{3+}/M^{2+} redox couple in $[M(CN)_6]$ in the PBA framework rather than the guest A ions, as described by Equation (5-6):

$$A_xT[M(CN)_6] + yY^{2+} \leftrightarrow A_xY_yT[M^{2+}(CN)_6]_{2y}[M^{3+}(CN)_6]_{1-2y} \quad (5)$$

$$\text{or } A_xT[M(CN)_6] + yY^{3+} \leftrightarrow A_xY_yT[M^{2+}(CN)_6]_{3y}[M^{3+}(CN)_6]_{1-3y} \quad (6)$$

5.3 Catalysts for the OER

The oxygen evolution reaction (OER) is a crucial part of water splitting, CO_2 reduction, and rechargeable metal-air batteries. Its sluggish reaction kinetics, however, hinders its further applications. Currently, the catalysts that have shown competitive performance are noble metals (Ir or Ru oxides), but the high price and scarcity of noble metals have motivated

researchers to develop new alternatives. The cheaper PBA compounds are considered as promising alternatives for the OER.[67-68, 74, 94, 109-110] Han et al. reported the OER performance of $Co_4[Fe(CN)_6]_{2.67}$ in neutral aqueous solution buffered at pH = 7 using a 0.1 M phosphate solution containing 1 M KNO_3 as supporting electrolyte.[109] There is a small reversible redox couple at potentials of 0.89/0.98 V that is assigned to the $Co^{2+/}Co^{3+}$ redox couple, and a pronounced catalytic wave appearing with a sharp onset at 1.15 V vs. normal hydrogen electrode (NHE), as shown in Figure 18(a). The effect of pH on the electrochemical stability of CoFe PBAs was investigated in the $1 < pH < 13$ range, and representative cyclic voltammograms (CVs) are shown in Figure 18(b). It is notable that the reversible $Co^{2+/}Co^{3+}$ redox couple and the onset potential of the OER was significantly dependent on the pH value. It was initially proposed that the electrocatalytic activity of PBAs comes from their high surface area and uniform porosity, which provide many active sites. Indra et al. investigated the catalytic mechanism of $Co[Co(CN)_6]$ PBAs through characterizing the catalyst after cyclic voltammetry measurements by X-ray photoelectron spectroscopy (XPS). The XPS results demonstrated that the PBAs are transformed into hydroxides-oxyhydroxides during the OER process in alkaline medium.[67] Su and co-authors investigated the active sites in $Na_xNiFe(CN)_6$ through operando spectroscopic studies including X-ray absorption spectroscopy (XAS).[74] They proposed a potential-dependent deprotonation reaction scheme, as shown in Figure 18(c). The as-prepared catalyst is completely transformed into amorphous nickel hydroxide ($Ni(OH)_2$) after the electrochemical reaction, and $Ni(OH)_2$ acts as the active species. When the $Na_xNiFe(CN)_6$ interacted with alkaline solution at low potential, partially oxidized Ni^{3+} species appeared owing to hydrogen atoms extracted from the hydroxyl groups. At higher potential, nickel ions were further oxidized to Ni^{4+} states due to the successive deprotonation. Theoretical calculations indicated that the Ni^{4+} triggers oxidized oxygen ions as electrophilic centres, with the subsequent activation of anion redox reactions for the OER.[74]

5.4 Hydrogen storage

Hydrogen is considered as an alternative to fossil fuel due to its clean combustion and high heating value. PBA compounds, as one kind of microporous coordination solid with three-dimensional frameworks and high surface areas, have been considered as suitable hosts for hydrogen storage.[64-66] Kaye et al. reported the hydrogen storage performance of the various PBAs with different transition metal ions and various amounts of vacancies. PBA compounds with the formula $T_3[M(CN)_6]_2$ have one-third hexacyanometalate vacancies due to the charge balance between T^{2+} and $[M(CN)_6]^{3-}$, resulting in more water molecules coordinating with metal centres. After removal of the water molecules by heat-treatment, unsaturated metal centres appear in the framework. Therefore, the hydrogen storage mechanism of PBAs is that the polarizable π-electron clouds of the cyanide bridges have some affinity for H_2, and the coordinatively unsaturated metal centres interact with H_2.[65] It was reported that the hydrogen storage capacity of PBAs is related to the kind of metal ion. Figure 19(a) shows the hydrogen storage isotherms for $T_3[Co(CN)_6]_2$ (T = Mn, Ni, Cu, Zn). It is significant that the $Cu_3[Co(CN)_6]_2$ has the best hydrogen storage capability, with a storage density of at least 0.029 kg H_2/L. Kaye et al. also proposed that the hydrogen storage capacity of PBAs has a strong dependence on the amount of vacancies.[64] $Cu_3[Co(CN)_6]_2$, $Fe_4[Fe(CN)_6]_3$, and $Ga[Co(CN)_6]$ with vacancy percentages of 33%, 25%, and 0%, respectively, were selected as subjects for investigation to test their hydrogen storage capacity. The results showed that the H_2 storage capacities increased with increasing concentration of $M(CN)_6$ vacancies in the PBA framework, varying from 1.4 wt% for $Ga[Co(CN)_6]$, to 1.6 wt% for $Fe_4[Fe(CN)_6]_3$ and 2.1wt% for $Cu_3[Co(CN)_6]_2$ (Figure 19(b)). It is concluded that the hydrogen storage capacity of PBAs is highly dependent on the concentrations of $M(CN)_6$ vacancies and T^{2+} cations.

6. Influence of structural and chemical properties on performance

6.1 Adverse influence of structural and chemical properties on applications

As mentioned above, there are some $M(CN)_6$ vacancies and zeolitic/coordinated water in the PBA framework, which will have some adverse influence on the electrochemical performance with respect alkaline ion and multivalent ion storage. Zeolitic water and alkaline ions have a competitive relationship towards occupying the octahedral centres of the subunits of the PBA framework. Moreover, there are some $M(CN)_6$ vacancies in the PBA framework, which will bring some water coordinated with metal ions into the PBA framework and reduce the number of alkaline ions in the PBA unit cell. Thus, if there is too much zeotilic and coordinated water in the framework, the number of alkaline ions in the PBA framework will consequently be reduced, resulting in low specific capacity for the alkaline ions and low initial coulombic efficiency. Our group prepared a series of $Na_xFeFe(CN)_6$ compounds with different amounts of sodium ions, that is, $Na_{1.26}Fe[Fe(CN)_6]\cdot 3.8H_2O$, $Na_{1.33}Fe[Fe(CN)_6]\cdot 3.5H_2O$, and $Na_{1.56}Fe[Fe(CN)_6]\cdot 3.1H_2O$. With more sodium ions in the PB framework, $Na_{1.56}Fe[Fe(CN)_6]\cdot 3.1H_2O$ (PB-5) delivered the highest capacity and initial coulombic efficiency of 115.6 mAh g^{-1} and 90.0%, respectively, compared with the other $Na_xFeFe(CN)_6$ PBAs (Figure 20(a)). Moreover, due to the presence of fewer defects in $Na_{1.56}Fe[Fe(CN)_6]\cdot 3.1H_2O$, its more stable structure shows better cycling performance (Figure 20(b)). In addition, the presence of H_2O affects the potential plateau in the charge-discharge curves. Goodenough's group tested the sodium ion storage performance of $Na_xMnFe(CN)_6$ samples that were heat-treated in air and under vacuum condition. The dehydrated $Na_xMnFe(CN)_6$, which was dried under vacuum conditions, showed a distinct potential plateau at 3.5 V, totally different from its counterpart dried under air (Figure 20(c, d)). In the case of multivalent-ion storage, the capacity is highly dependent on the M^{3+}/M^{2+} redox couple in $[M(CN)_6]$ rather than the guest ions (A) in the PBA framework. Therefore, if the PBA compounds contain more $[M(CN)_6]$ vacancies, they will deliver less capacity for multivalent-ion storage (Mg^{2+}, Ca^{2+}, Zn^{2+}, Ba^{2+}).

Therefore, in order to obtain excellent electrochemical performance from PBAs for alkaline ions and multivalent-ion storage, it is necessary to adopt some strategies to reduce the amount of water and $M(CN)_6$ vacancies in the PBAs. The strategies include: 1) coarsening the PBAs particles to reduce the adsorbed surface area; 2) dehydrating PBAs samples at higher temperature under high vacuum conditions; 3) introducing more alkaline ions into the PBA framework to reduce the adsorption sites for zeolitic water through increasing the proportion of alkaline ions in the reaction solution; 4) reducing the rate of chemical reactions, consequently decreasing the amount of $M(CN)_6$ vacancies; and 5) utilizing a chelating agent that can coordinate with metal ions to slow down the reaction rate to obtain high quality PBAs.

6.2 Favourable influence of structural and chemical properties on applications

Although the presence of $[M(CN)_6]$ vacancies is detrimental to the electrochemical performance of alkaline ion batteries and multivalent ion batteries, it is favourable for H_2 storage because the $[M(CN)_6]$ vacancies can act as sites where H_2 is absorbed on unsaturated metal. Thus, introducing more vacancies into the PBA framework would absorb more H_2. Thus, for hydrogen storage application, PBAs compounds are required to contain more $[M(CN)_6]$ vacancies. To increase these vacancies in the PBA framework, some strategies include: 1) Introducing more the zeolitic water into the PBA framework through decreasing the concentration of alkaline ions in the reaction solution and then dehydrating the zeolitic water with an appropriate heating method to obtain defect-rich PBAs that are not vulnerable to structure collapse. 2) Speeding up the rate of chemical reaction, which consequently increases the amount of $M(CN)_6$ vacancies in PBAs framework. 3) Avoiding the use of chelating agents during the PBA synthesis to produce defect-rich PBA compounds.

7. Conclusions and Perspectives

In summary, we have provided a comprehensive review on the structural and chemical properties of PBA frameworks, and their applications in alkaline ion batteries (LIBs, SIBs, KIBs), multi-valent ion batteries (Mg^{2+}, Ba^{2+}, Ca^{2+}, Zn^{2+}), hydrogen storage, and

electrocatalysts (OER), along with a discussion of the influence of chemical and structural properties on their applications. Owing to their environmental friendliness and low-cost precursors, PBAs are considered as promising candidates for batteries, especially the Mn-based and Fe-based PBAs. The presence of zeolitic/coordinated water in PBA frameworks, however, is detrimental to their initial coulombic efficiency and specific capacity. Moreover, the zeolitic/coordinated water will be extracted from PBA framework during the first cycle, damaging the organic electrolyte. Considering this point, there is some concerns relating the commercial application of PBAs for organic electrolyte batteries. In comparison, applying PBAs as cathode materials for aqueous batteries need not take this concern into account. In addition, aqueous batteries possess high rate capability, long cycling life, and high safety. Thus, PBAs used as cathode for aqueous batteries are likely to become an attractive topic for investigation, and more new PBA framework with low vacancies need to be developed.

In terms of nanostructure synthesis, PBAs are good templates to prepare various morphologies of metal oxides, metal sulphides, and metal phosphides. For application as electrocatalysts, due to their instability in acid or alkaline solutions, PBAs are only suitable as catalysts for use in neutral electrolyte. The application of PBAs in the field of multivalent-ion batteries represents a new research direction, but it is still in its early stages. In the future, further investigation needs to be undertaken, such as on the storage mechanism of PBAs and the development of new PBA frameworks with long cycle life.

Acknowledgements

This work was supported by a Discovery Early Career Researcher Award (DECRA, No. DE180101478) of the Australian Research Council and an Australian Renewable Energy Agency (ARENA) Project (No. G00849). The authors would like to also thank Dr. Tania Silver for her critical reading of the manuscript.

References

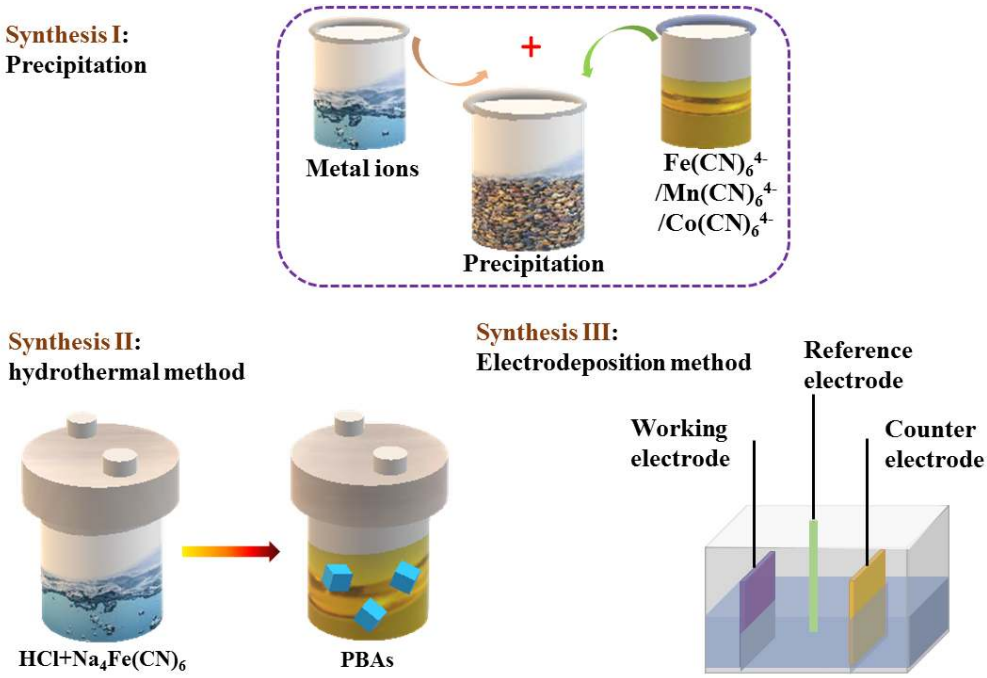

Figure 1. Synthesis methods for Prussian blue analogues (PBAs).

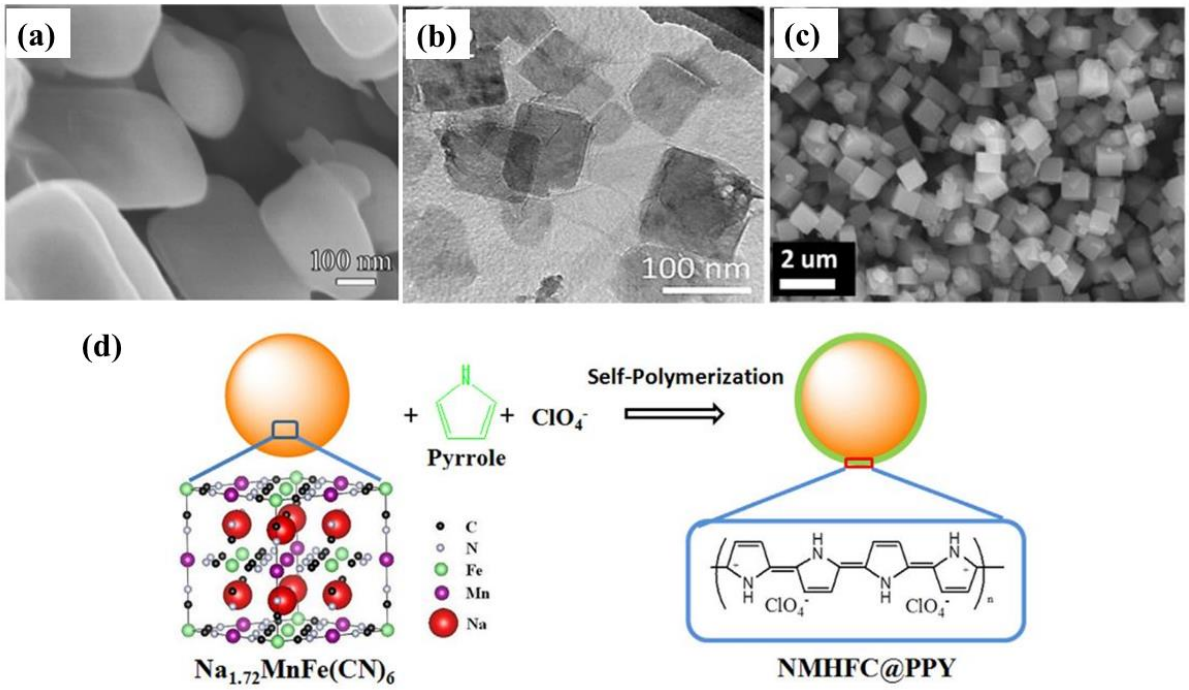

Figure 2. The morphologies of PBAs prepared via the precipitation method: (a) random morphology; Reproduced with permission. [63] Copyright 2015, Elsevier. (b) nanoflakes; Reproduced with permission. [69] Copyright 2013, Royal Society of Chemistry. (c) nanocubes. Reproduced with permission.[44] Copyright 2016, American Chemical Society. (d) schematic illustration of synthesis of $Na_{1.72}MnFe(CN)_6$@PPy (NMHFC@PPy). Reproduced with permission. [63] Copyright 2015, Elsevier.

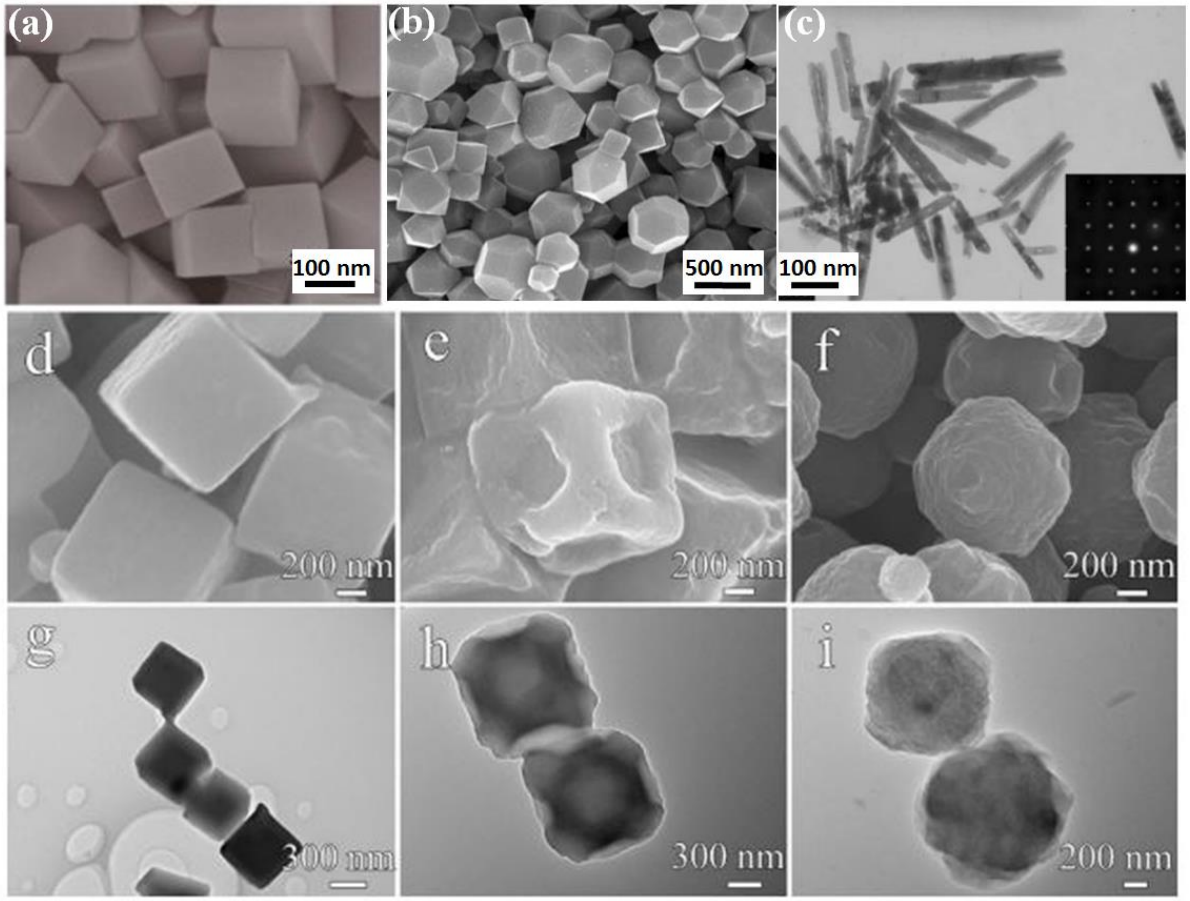

Figure 3. (a) $Na_xFe[Fe(CN)_6]$ nanocubes, Reproduced with permission.[33] Copyright 2014, Royal Society of Chemistry. (b) $Co_3[Co(CN)_6]_2$ polyhedra and (c) $Co_3[Co(CN)_6]_2$ nanorods with the corresponding selected area electron diffraction (SAED) pattern in the inset. Reproduced with permission.[81] Copyright 2005, Royal Society of Chemistry. Field emission scanning electron microscope (FE-SEM) images of d) PB-1mL HCl, e) PB-2mL HCl and f) PB-3mL HCl. Transmission electron microscope (TEM) images of g) PB-1mL HCl, h) PB-2mL HCl, and i) PB-3mL HCl. Reproduced with permission.[51] Copyright 2017, Wiley-VCH.

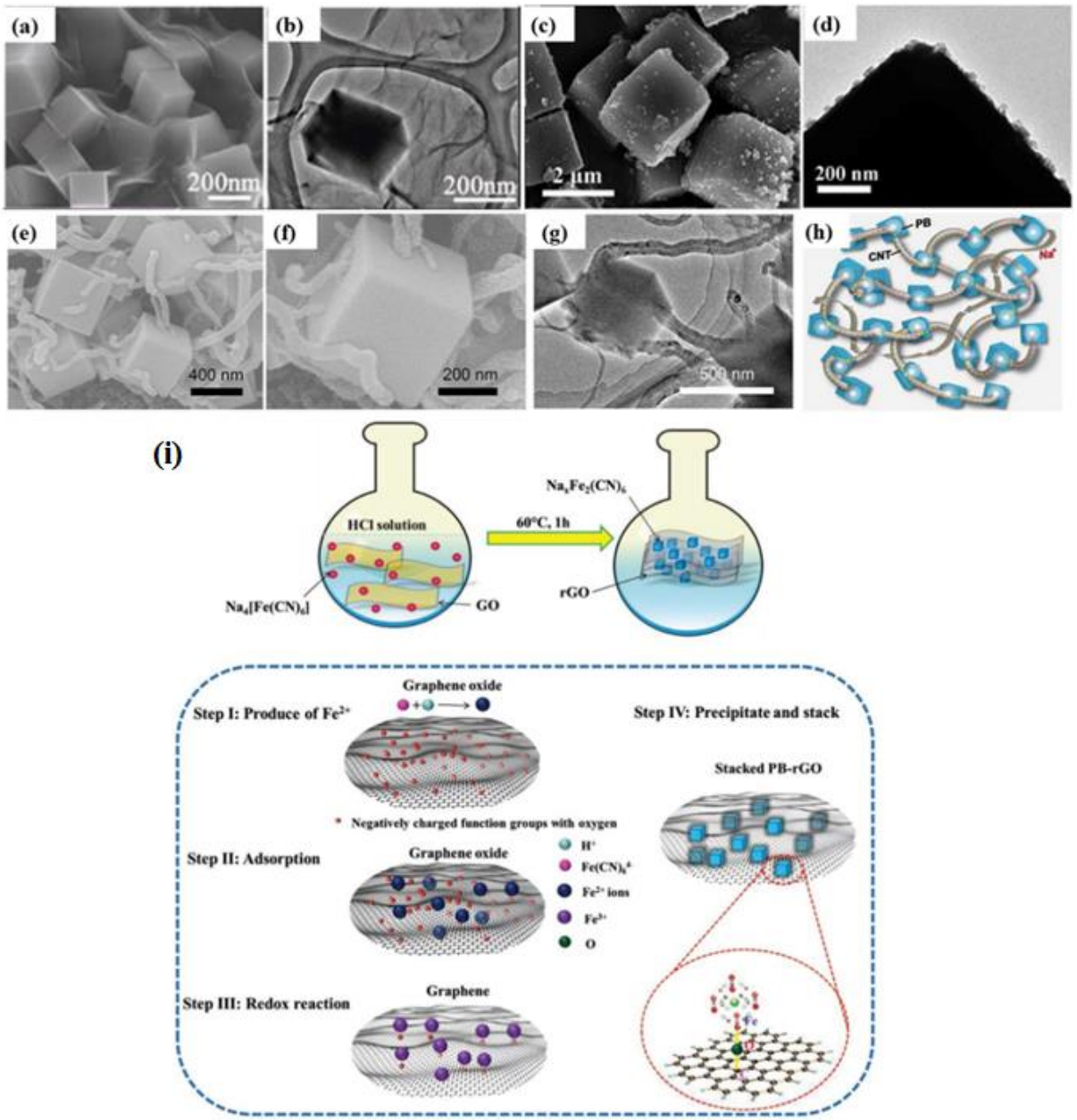

Figure 4. (a, b) PB/rGO composite; Reproduced with permission.[59] Copyright 2018, Wiley-VCH. (c, d) PB/PPy composite; Reproduced with permission.[42] Copyright 2016, Royal Society of Chemicstry. (e-h) PB/CNT composite. Reproduced with permission.[45] Copyright 2016, Wiley-VCH. (a, c, e, f) SEM images, (b, d, g) TEM images, and (h) schematic diagram of the structure of PB/CNT. (i) Synthetic process and reaction mechanism for the PB-rGO composite. Reproduced with permission. [59] Copyright 2018, Wiley-VCH.

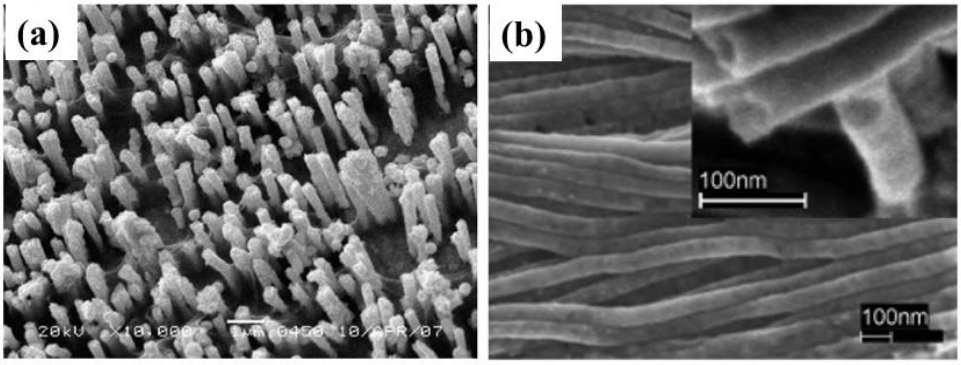

Figure 5. (a) Prussian blue nanowires, Reproduced with permission.[83] Copyright 2007, Elsevier.and (b) nanotubes prepared by electrodeposition, with higher magnification shown in the inset. Reproduced with permission.[85] Copyright 2005, American Chemical Society.

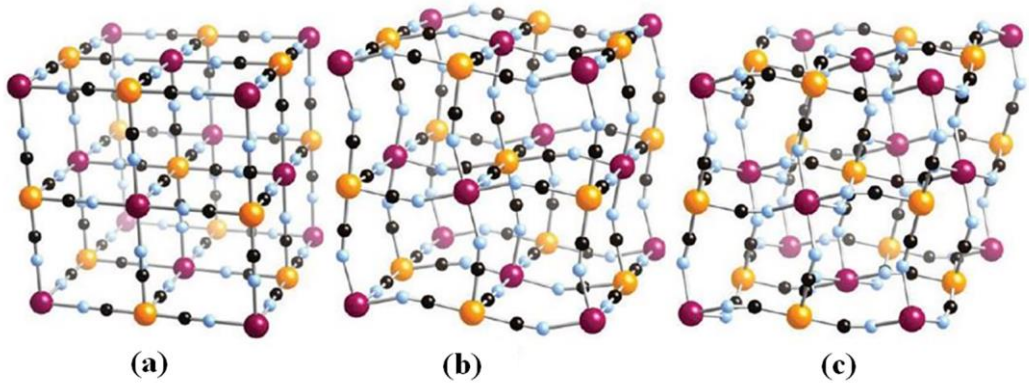

Figure 6. $Cs_2Mn[Mn(CN)_6]$ structures: (a) cubic (b) monoclinic, and (c) rhombohedral. Reproduced with permission.[111] Copyright 2012, American Chemical Society.

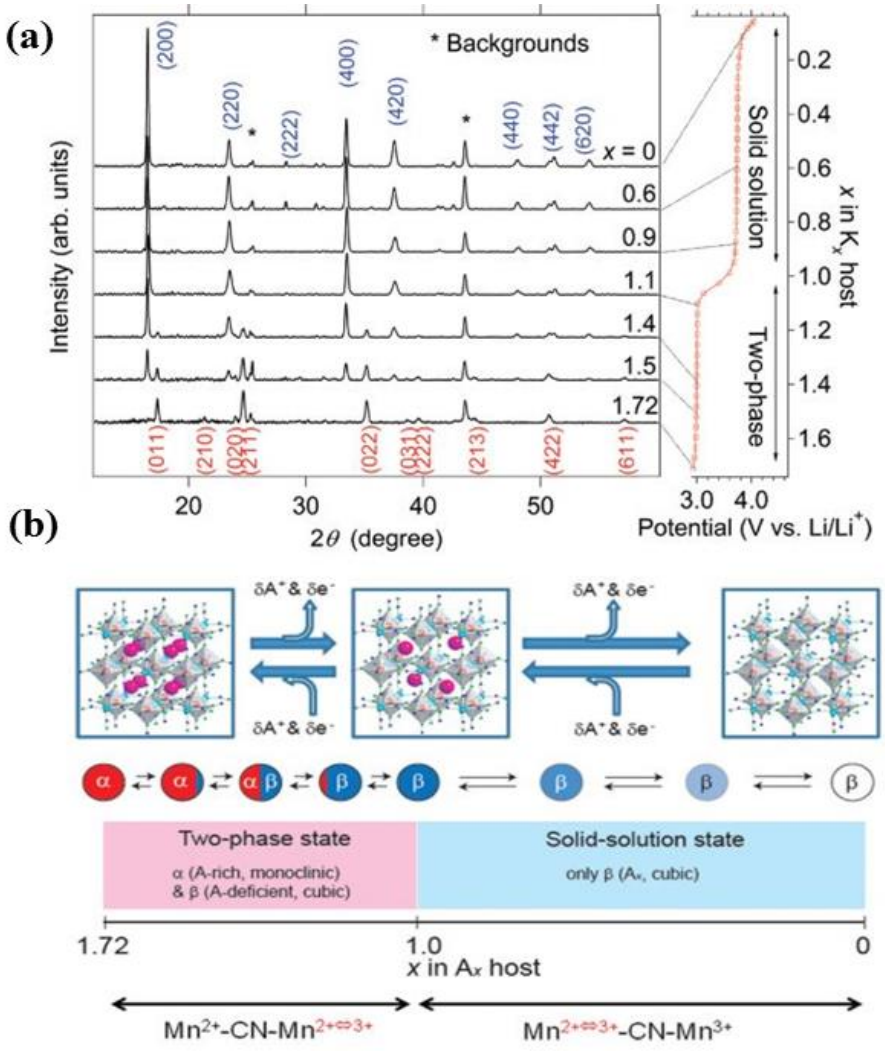

Figure 7. (a) X-ray diffraction (XRD) patterns and (b) structural evolution of $A_xMn[Mn(CN)_6]\cdot 0.65H_2O$ with different amounts of alkaline ions (x). Crystal structures for x = 1.72, 1.0, and 0 (top). In the middle, a schematic diagram of the structural changes for a particle is displayed. At the bottom, the redox reactions for the Mn-CN-Mn framework are shown. Reproduced with permission.[25] Copyright 2012, American Chemical Society.

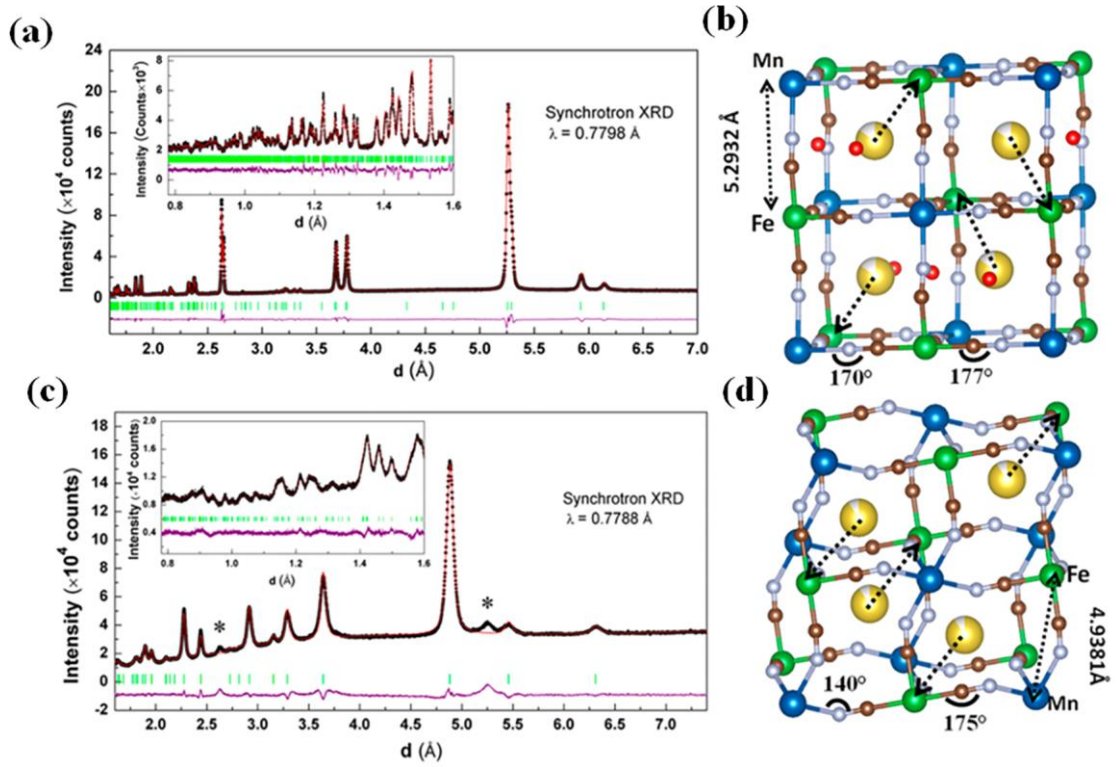

Figure 8. Synchroton X-ray diffraction (SXRD) patterns of (a) monoclinic $Na_{2-\delta}MnFe(CN)_6$ and (c) rhombohedral $Na_{2-\delta}MnFe(CN)_6$, with the insets showing an enlargement of the indicated range. Local structures of (b) monoclinic $Na_{2-\delta}MnFe(CN)_6$ and (d) rhombohedral $Na_{2-\delta}MnFe(CN)_6$, showing the Na^+ displacements and the distorted framework. In (a) and (c), the black dots show the observed data, the red lines are the calculated patterns, the purple lines correspond to the difference between the observed and calculated patterns, and the vertical green bars are the expected positions of Bragg reflections. Asterisks in (c) show peaks from absorbed water during the sample preparation for SXRD. In (b) and (d), high-spin Mn^{II} is blue, low-spin Fe^{II} is green, N is silver, C is dark brown, Na is yellow, and O is red. Reproduced with permission.[36] Copyright 2015, American Chemical Society.

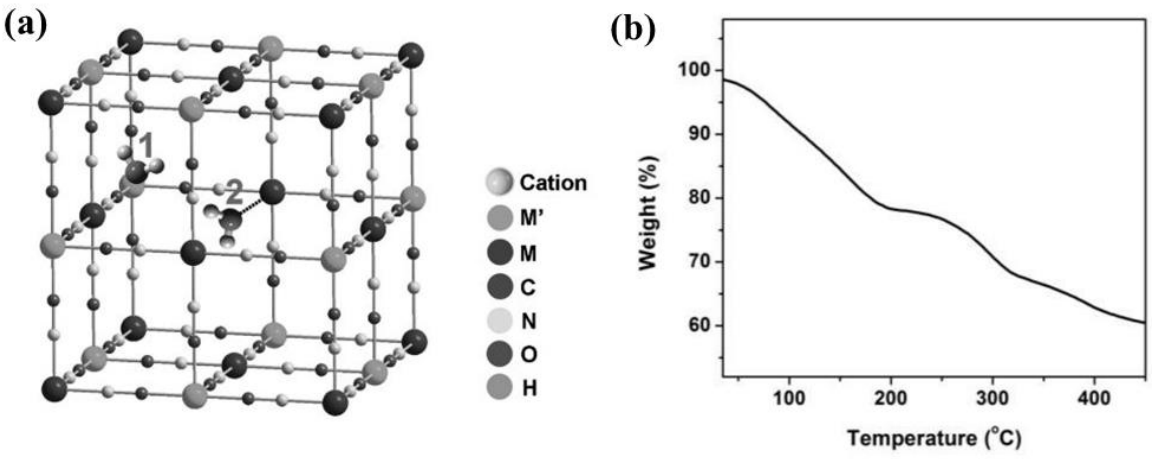

Figure 9. (a) Positions of zeolite water and coordinated water, and (b) TGA curve of the $K_xFeFe(CN)_6$. Reproduced with permission.[86] Copyright 2016, Wiley-VCH.

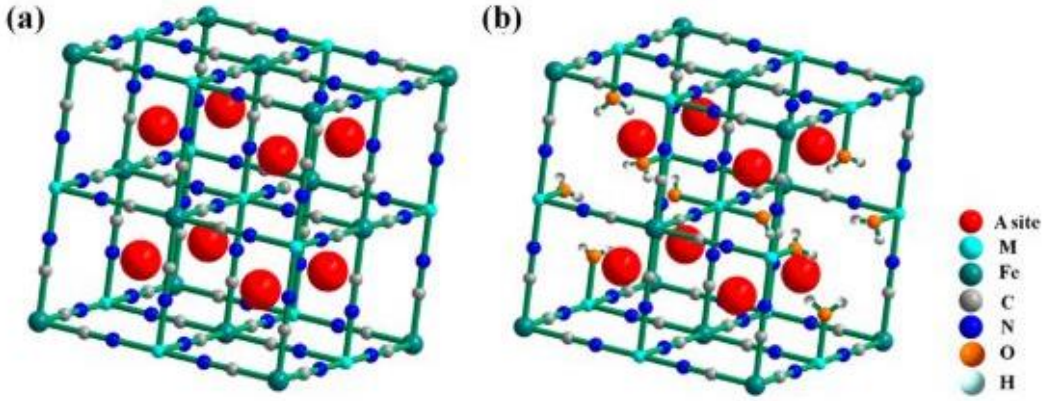

Figure 10. Crystal structures of Prussian blue framework without (a) and (b) with $Fe(CN)_6$ vacancies. Reproduced with permission.[43] Copyright 2016, American Chemical Society.

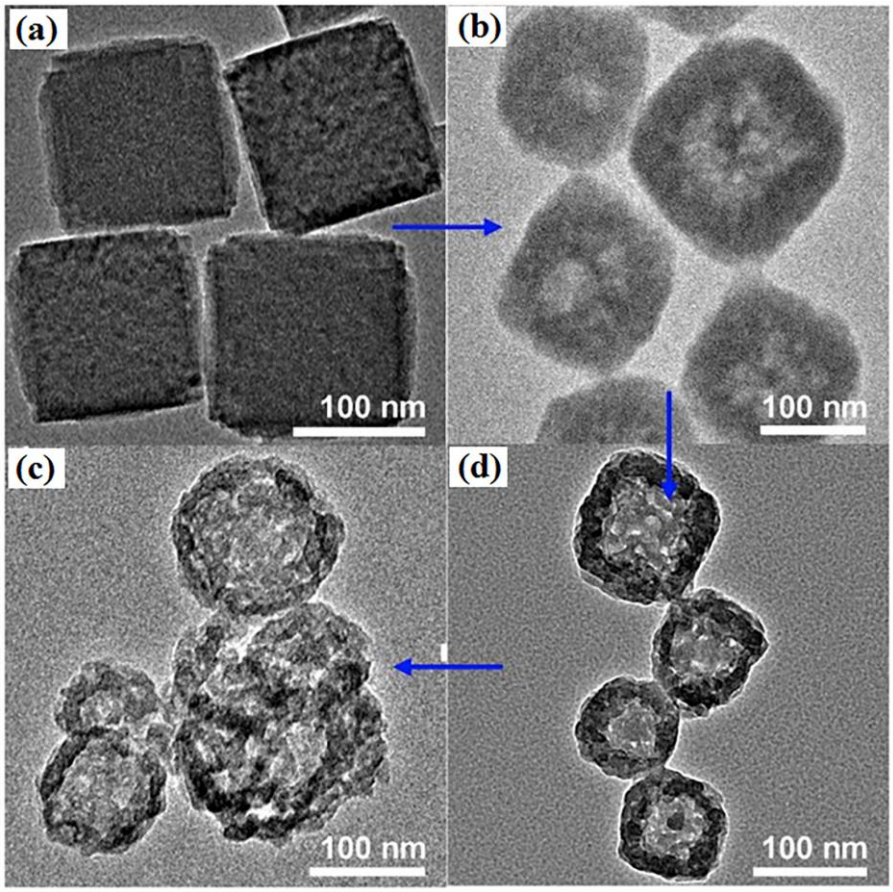

Figure 11. Morphology evolution of PB mesocrystals in HCl solution with applied etching time of (a) 0 min, (b)3.5 h, (c) 4.0 h, and (d)4.5 h. Reproduced with permission.[89] Copyright 2012, Wiley-VCH.

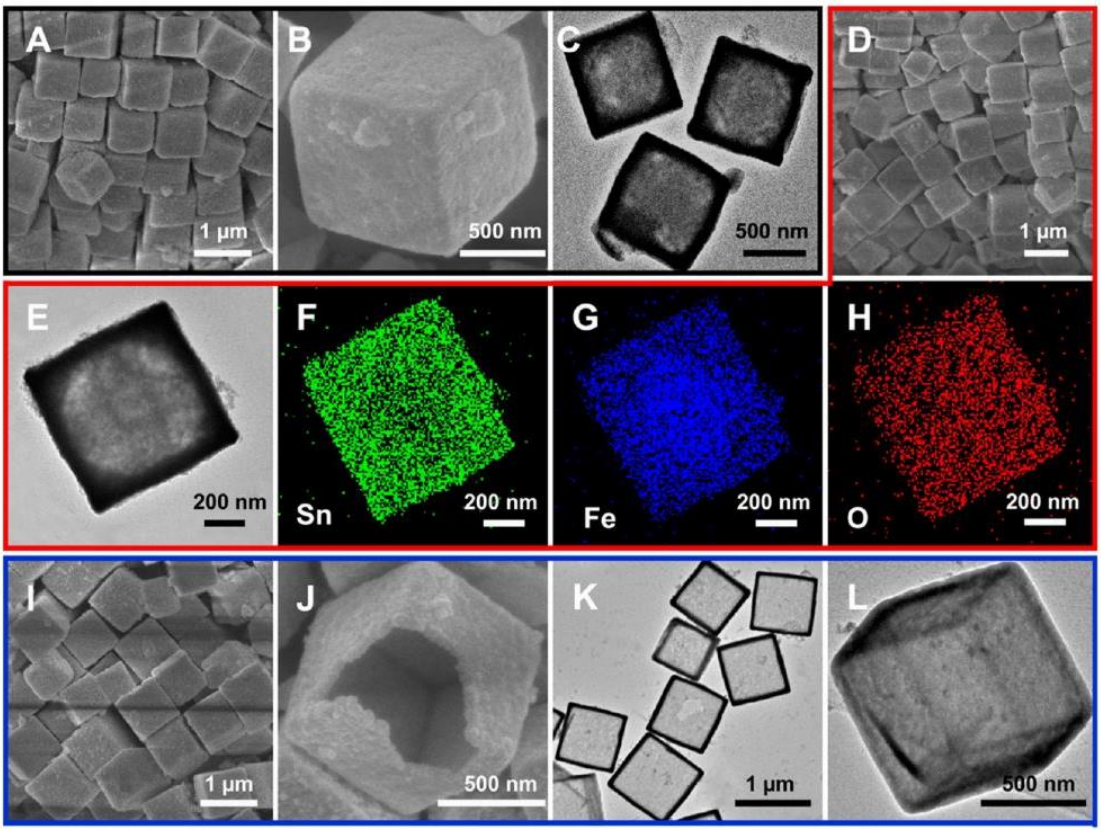

Figure 12. Formation of composite Fe_2O_3/SnO_2 microboxes by PB templating at room temperature: field emission scanning electron microscope (FESEM) (A, B) and TEM (C) images of $Fe(OH)_3/SnO_2{\cdot}xH_2O$ microboxes; FESEM (D), TEM (E) image, and EDX-element mapping images (F-H) of the Fe_2O_3/SnO_2 microbox shown in (E), FESEM (I, J) and TEM (K, L) images of SnO_2 microboxes. Reproduced with permission.[87] Copyright 2013, American Chemical Society.

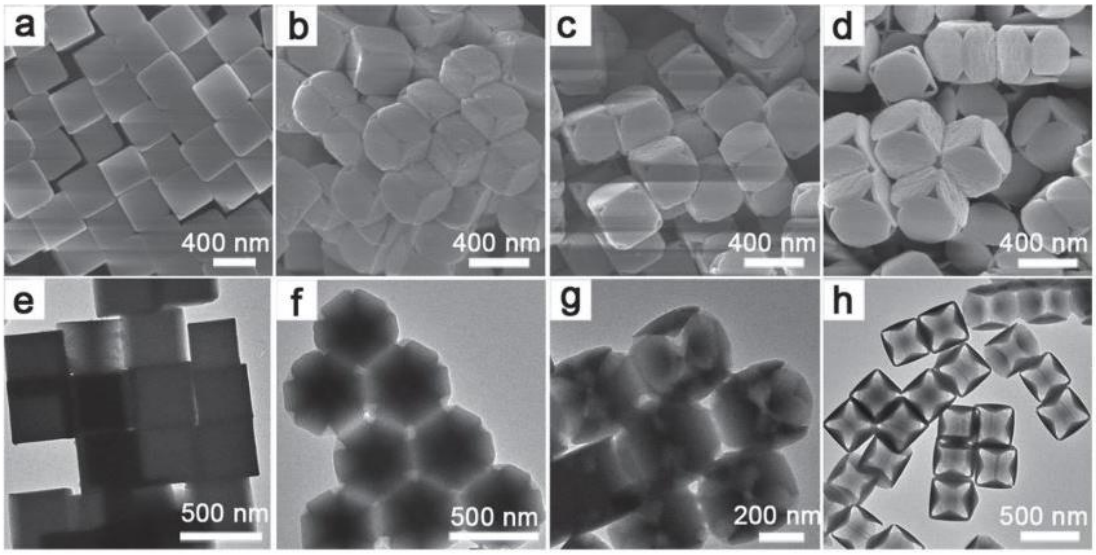

Figure 13. a-d) FESEM and (e-h) TEM images of the etching products obtained after reacting 20 mg of Ni-Co PBA cubes with 2.5 mL ammonia at room temperature for (a, e) 0 h, (b, f) 0.5 h, (c, g) 2 h, and (d, h)6 h. Reproduced with permission. [88] Copyright 2016, Wiley-VCH.

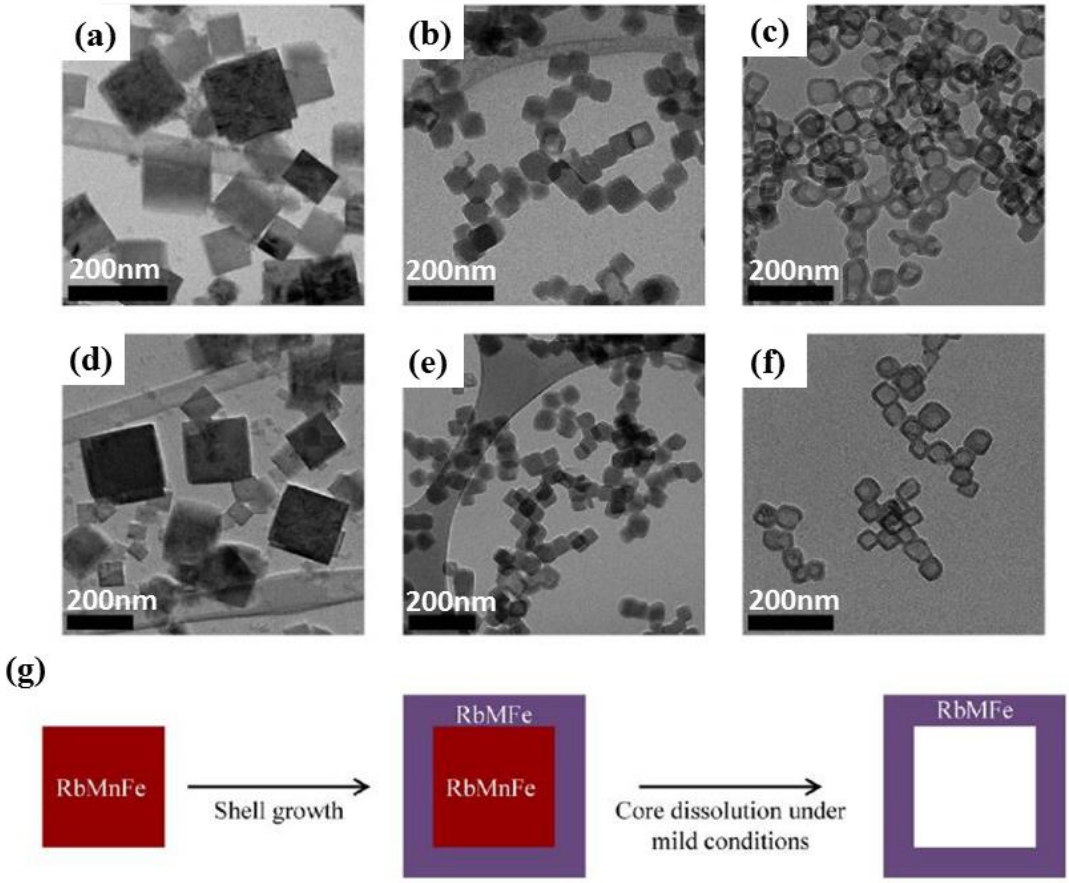

Figure 14. TEM images of RbMnFe cores (a, d), showing polydispersed cubes with a size range of 50 to 300 nm; (b) uniform cubic core@shell particles of RbMnFe@RbCoFe and (e) RbMnFe@RbNiFe; (c) RbCoFe and (f) RbNiFe hollow shells with their shape and size preserved on removal of the template the shell thickness ranges from 9 to 15 nm; (g) the synthetic strategy, in which involves preparing core@shell heterostructures with a RbMnFe core as a template and RbMFe (M = Co, Ni) as a shell. Reproduced with permission.[96] Copyright 2013, American Chemical Society.

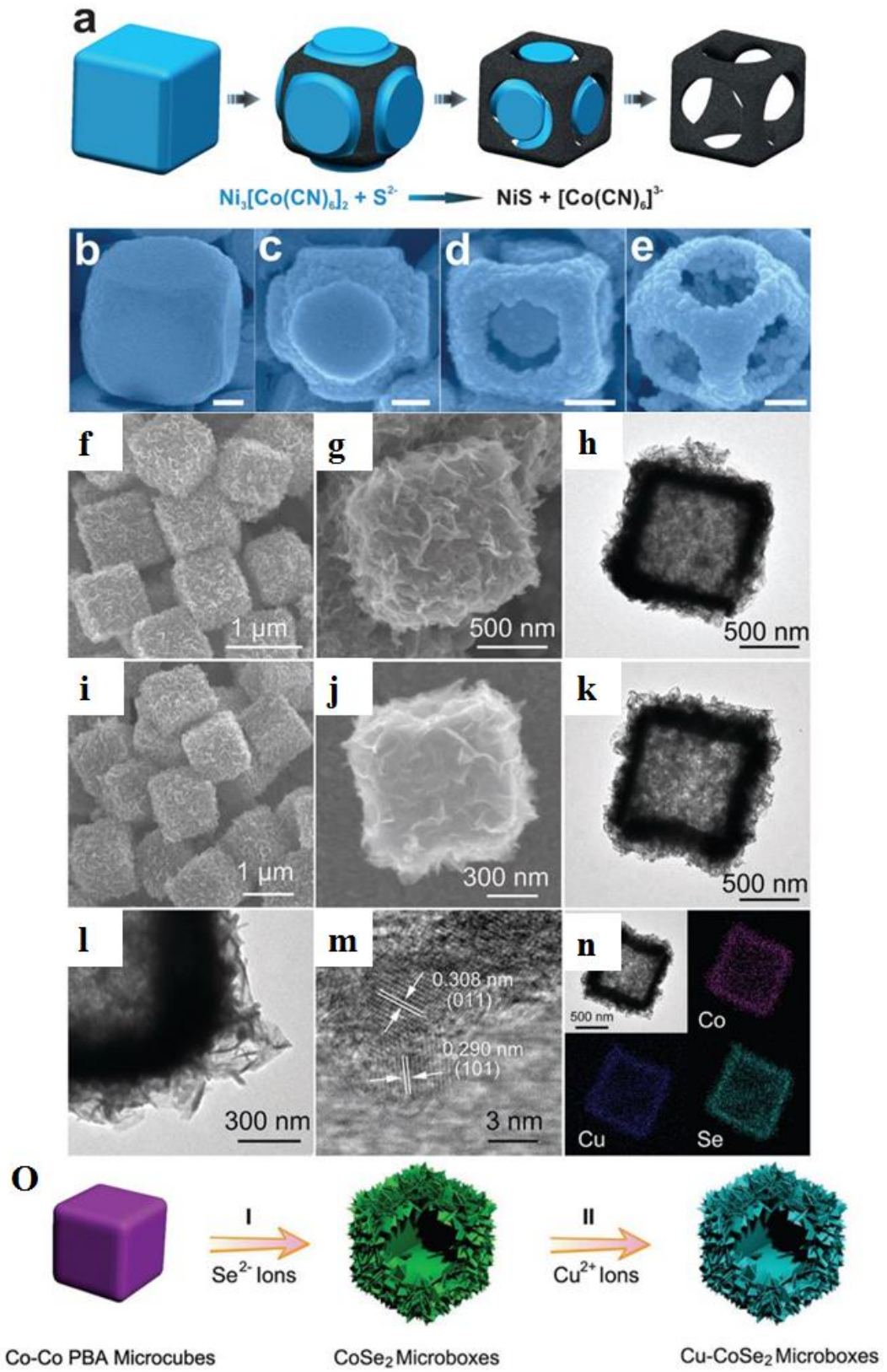

Figure 15. a) Schematic illustration of the formation process of NiS nanoframes. 20 mg of Ni-Co PB analogue nanocubes were reacted with 40 mg of Na_2S at 100 ºC for different durations. b–e) FESEM images of the products obtained after reaction for b) 0 h, c)0.5 h, d) 2

h, and e) 6 h. Scale bars: 100 nm. (f, g) Typical FESEM images and h) TEM image of the $CoSe_2$ microboxes. (i, j) FESEM images, (k, l) TEM images, and (m) high resolution TEM (HRTEM) image of Cu–$CoSe_2$ microboxes. (n) Scanning TEM (STEM) image and corresponding elemental mapping images of Co, Cu, and Se elements. (o) Schematic illustration of the two-step ion-exchange reaction for the synthesis of Cu–$CoSe_2$ microboxes. Figure 17 (a-e) reproduced with permission.[98] Copyright 2015, Wiley-VCH. Figure 17 (f-o) reproduced with permission.[97] Copyright 2018, Wiley-VCH.

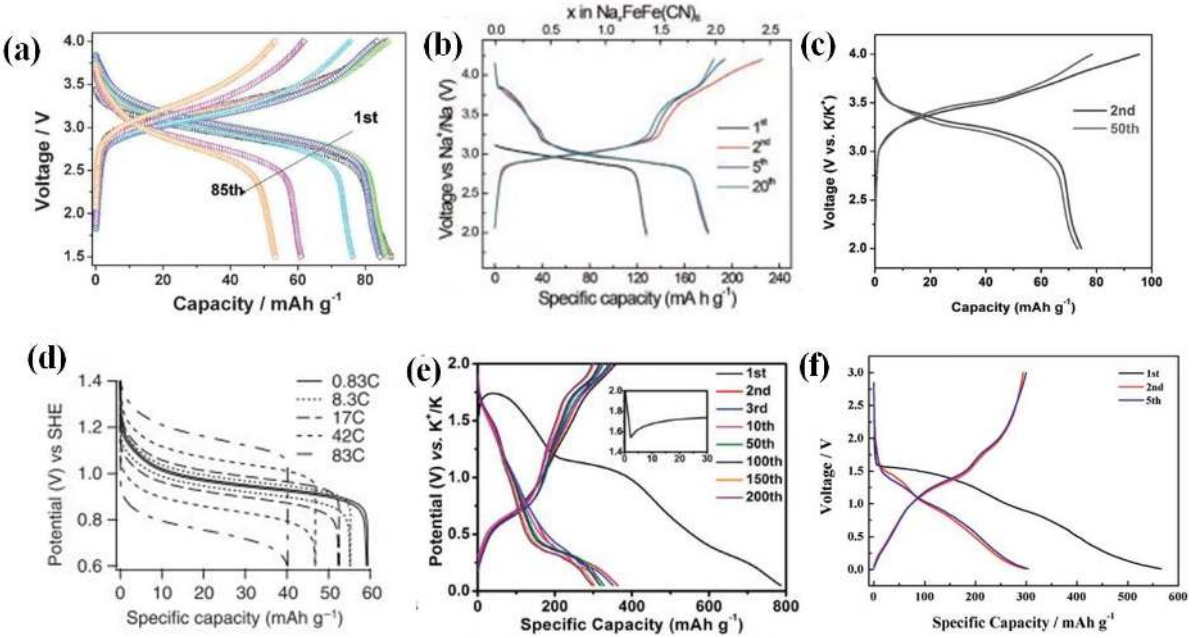

Figure 16. (a-d) Charge-discharge curves of PBAs used as cathode: (a) $FeFe(CN)_6$ in LIBs, Reproduced with permission.[103] Copyright 2014, Wiley-VCH. (b) $FeFe(CN)_6$ for Na, Reproduced with permission [33]. Copyright 2014, Royal Society of Chemistry. (c) $KFeFe(CN)_6$ for K in organic electrolyte, Reproduced with permission.[86] Copyright 2017, Wiley-VCH. and (d) K-ion battery with aqueous electrolyte, Reproduced with permission.[22] Copyright 2011, Nature.; (e-f) charge-discharge curves of PBAs used as anode for (e) K-ion battery in organic electrolyte, Reproduced with permission.[104] Copyright 2018, Wiley-VCH.; and (f) charge-discharge curves of $Co_3[Co(CN)_6]_2$ in a Li-ion battery. Reproduced with permission.[105] Copyright 2014, Royal Society of Chemistry.

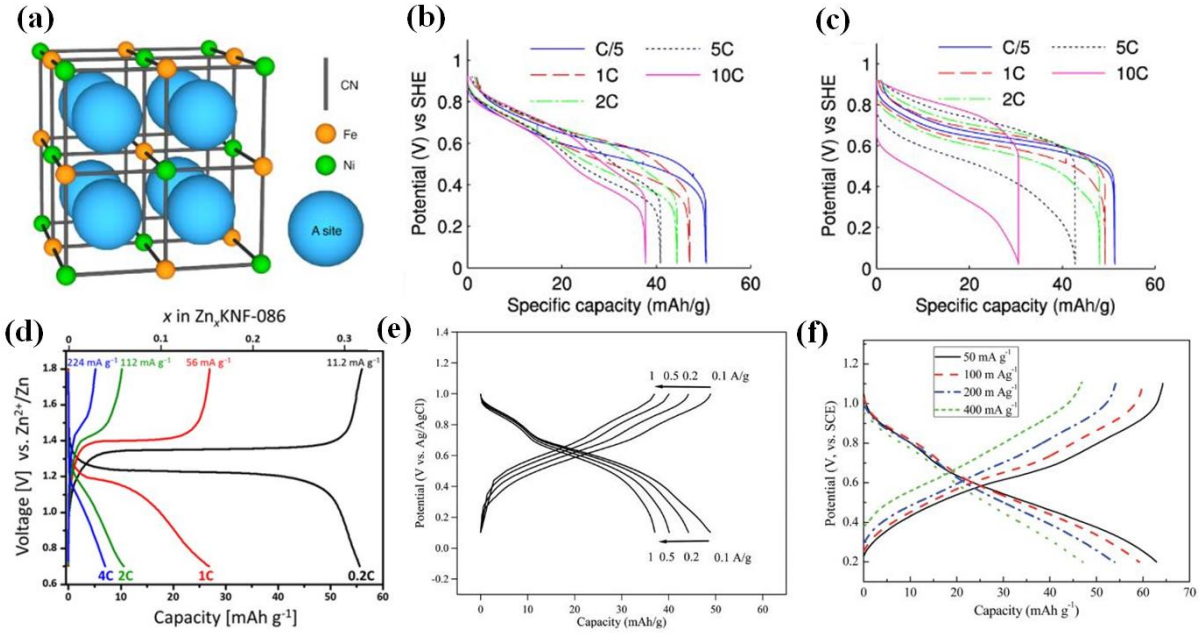

Figure 17. (a) The open channels in the <100> direction of $K_xNiFe(CN)_6$ as shown in structure allow for rapid insertion and extraction of a variety of cations. [106] (b-d) $K_xNiFe(CN)_6$ open framework for (b) Ca^{2+}, [106] (c) Ba^{2+},[106] Reproduced with permission. [106] Copyright 2013, American Chemical Society. and (d) Zn^{2+} storage, [112] respectively. Reproduced with permission. [112] Copyright 2017, Elsevier. Charge-discharge curves of CuFe-PB for (e) Mg ion batteries, Reproduced with permission.[107] Copyright 2013, Royal Society of Chemistry. (f) Al ion batteries in 0.5 M $Al_2(SO_4)_3$ aqueous solution. Reproduced with permission.[108] Copyright 2015, Royal Society of Chemistry.

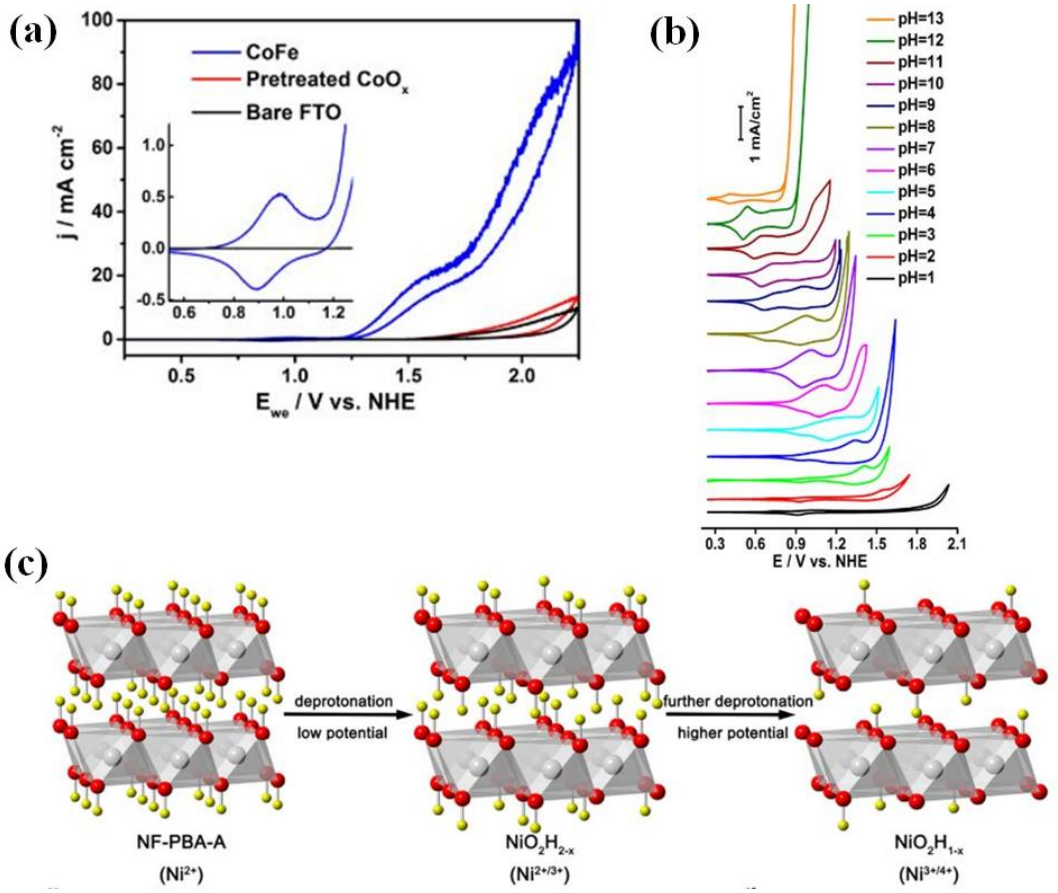

Figure 18. (a) Cyclic votammograms of CoFe PBAs in buffer solution at pH = 7, with the inset showing an enlargement of the indicated voltage range;[109] (b) representative CVs of CoFe-PB electrode at a scan rate of 5 mV/s at various pH values.[109] Reproduced with permission.[109] Copyright 2016, American Chemical Society. (c) multistep deprotonation of $Na_xNiFe(CN)_6$ during the OER. [74] Reproduced with permission. [74] Copyright 2018, American Chemical Society.

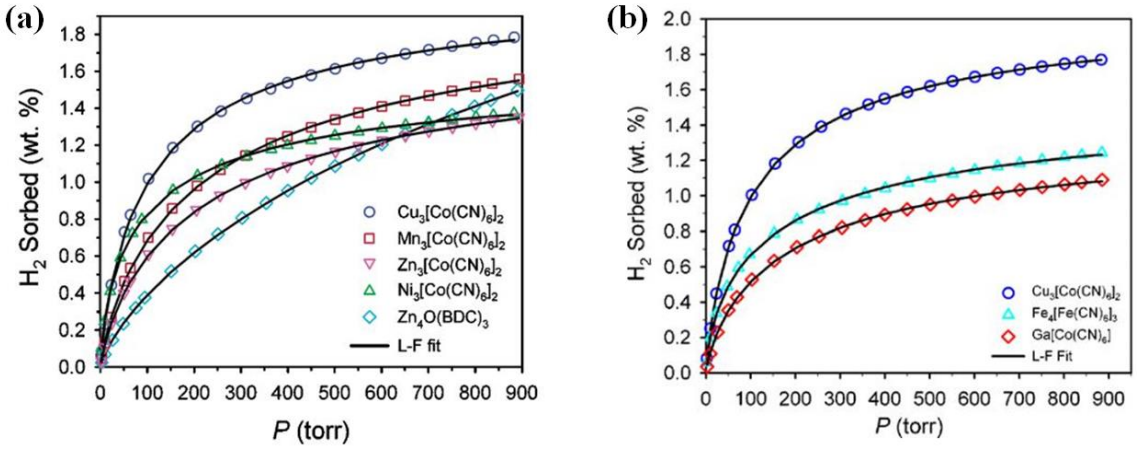

Figure 19. Hydrogen sorption isotherms for the Prussian blue analogues (a) $T_3[Co(CN)_6]_2$ (T = Mn, Ni, Cu, Zn),[65] Reproduced with permission.[65] Copyright 2005, American Chemical

Society. and (b) $Cu_3[Fe(CN)_6]_2$, $Fe_4[Fe(CN)_6]_3$, $Ga[Co(CN)_6]$ with different amount of vacancies.[64] Reproduced with permission. [64] Copyright 2007, Elsevier.

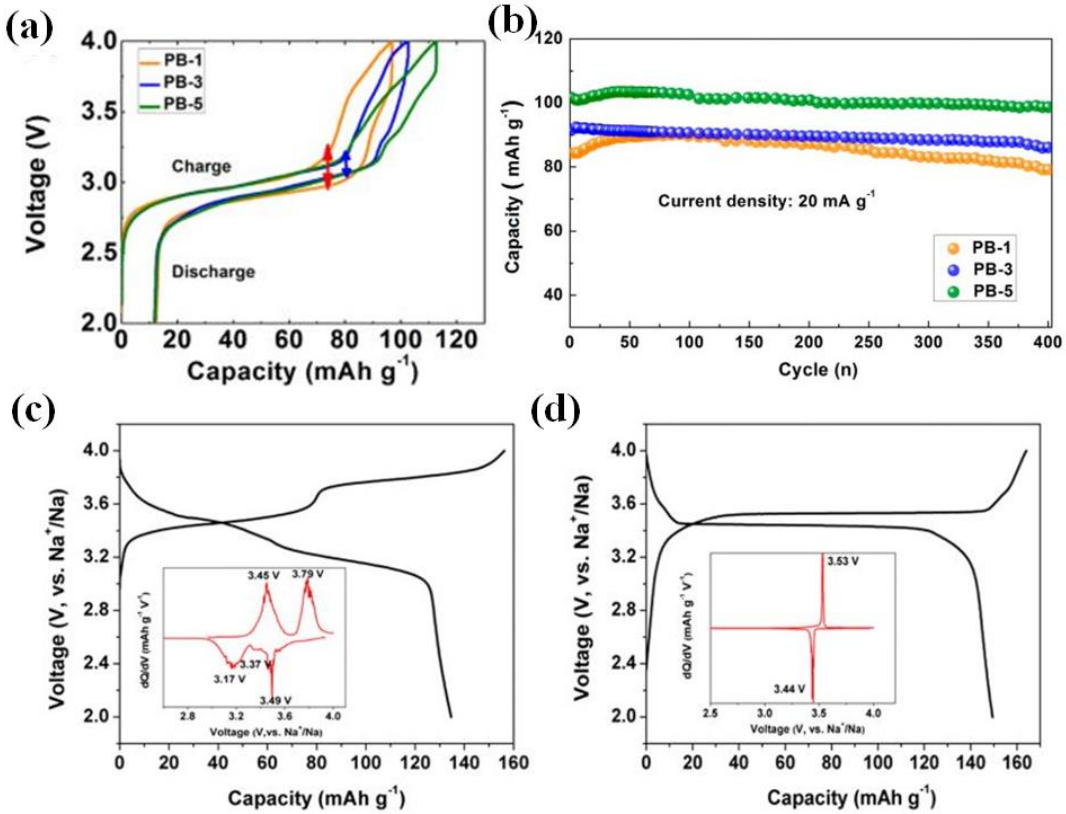

Figure 20. (a) Charge-discharge curves and (b) cycling performance of $Na_xFeFe(CN)_6$ frameworks with different amounts of H_2O. Reproduced with permission.[8] Copyright 2005, American Chemical Society. (c-d) Charge-discharge curves of $Na_xMnFe(CN)_6$ heat-treated in (c) air and (d) vacuum, with corresponding differential capacity curves in the insets.[36] (PB-1: $Na_{1.26}Fe[Fe(CN)_6]\cdot 3.8H_2O$, PB-3: $Na_{1.33}Fe[Fe(CN)_6]\cdot 3.5H_2O$, PB-5: $Na_{1.56}Fe[Fe(CN)_6]\cdot 3.1H_2O$). Reproduced with permission. [36] Copyright 2005, American Chemical Society.

Table 1. List of the performance characteristics of the representative PBAs for alkaline-ion batteries. KIB: potassium ion battery; SIB: sodium ion battery; SHE: standard hydrogen electrode.

Samples	Application	Capacity (mAh g^{-1})	Current density (mA g^{-1})	Potential (V)	Cycling stability
$Mn_3[Co(CN)_6]_2$[105]	Anode for LIBs	868.2	50	0.83 vs. Li^+/Li	35.3 mAh g-1 after 100 cycles
$Co_3[Co(CN)_6]_2$[105]	Anode for LIBs	566.2	20	1.06 vs. Li^+/Li	304 mAh g-1 after 5 cycles
$Fe_4[Fe(CN)_6]_3$[103]	Cathode for	95	25	3.0 vs.	75%

	LIBs			Li^+/Li	retention after 50 cycles
$FeFe(CN)_6$[103]	Cathode for LIBs	138	25	3.0 vs. Li^+/Li	70% retention after 50 cycles
$LiFeFe(CN)_6$[100]	Cathode for LIBs	142	71	3.0 vs. Li^+/Li	85% retention after 200 cycles
$FeFe(CN)_6$[43]	Cathode for LIBs	160	25	3.0 vs. Li^+/Li	90% retention after 300 cycles
$FeFe(CN)_6$[113]	Cathode for KIBs	125	0.5 C	3.3 vs. K^+/K	95% retention after 100 cycles
$K_{0.22}Fe[Fe(CN)_6]_{0.805}\cdot 4.0H_2O$[86]	Cathode for KIBs	76.7	50	3.18 vs. K^+/K	94% retention after 50 cycles
$Co_3[Co(CN)_6]_2$[104]	Anode for KIBs	324.5	100	1.17 and 0.32 V vs. K^+/K	82% retention after 200 cycles
PB/MoS_2[114]	Cathode for aqueous KIBs	215	1000	0.5 V vs. Ag/AgCl	97% retention after 10000 cycles
$K_{0.6}Ni_{1.2}Fe(CN)_6\cdot 3.6H_2O$[23]	Cathode for aqueous KIBs	60	1 C	0.69 V vs. SHE	98.25% retention after 1000 cycles
$KCuFe(CN)_6$ [22]	Cathode for aqueous KIBs	59.14	0.83	0.95V vs. SHE	67% retention after 100 cycles
$K_2FeFe(CN)_6$[48]	Cathode for KIBs	140	10	3.1 vs. K^+/K	60% retention after 300 cycles
$K_{1.89}Mn[Fe(CN)_6]_{0.92}\cdot 0.75H_2O$[55]	Cathode for KIBs	142	1C	3.6 vs. K^+/K	-
$K_{1.75}Mn[Fe(CN)_6]_{0.93}\cdot 0.16H_2O$[46]	Cathode for KIBs	141	30	3.8 vs. K^+/K	92% retention after 100 cycles
$Na_{1.92}Fe_2(CN)_6$[37]	Cathode for SIBs	160	75	3.3 vs. Na^+/Na	75% after 1000 cycles
$Na_{1.56}Fe[Fe(CN)_6]\cdot 3H_2O$[8]	Cathode for SIBs	103.6	20	3.0 vs. Na^+/Na	97% after 400 cycles
$Na_{0.61}Fe[Fe(CN)_6]_{0.94}$[33]	Cathode for SIBs	170	25	3.0 vs. Na^+/Na	99.3% after 150

					cycles
$Na_{0.65}Fe[Fe(CN)_6]@C$[40]	Cathode for SIBs	130	50	3.0 vs. Na^+/Na	90% after 2000 cycles
$NaFe[Fe(CN)_6]@CNT$[45]	Cathode for SIBs	167	0.1C	3.0 vs. Na^+/Na	79.2% after 1000 cycles
$Na_{0.81}Fe[Fe(CN)_6]_{0.79}@rGO$[38]	Cathode for SIBs	131.2	30	2.8 vs. Na^+/Na	91.9 % after 500 cycles
$Na_{1.72}MnFe(CN)_6$[29]	Cathode for SIBs	134	6	3.6 vs. Na^+/Na	89.5% after 30 cycles
$Na_{1.40}MnFe(CN)_6$[29]	Cathode for SIBs	111	6	3.6 vs. Na^+/Na	95.9% after 30 cycles
$Na_{1.76}Ni_{0.12}Mn_{0.88}[Fe(CN)_6]_{0.98}$[32]	Cathode for SIBs	123.3	10	3.2 vs. Na^+/Na	83.8% after 2000 cycles
$Na_{1.72}MnFe(CN)_6@PPy$[63]	Cathode for SIBs	124	10	3.6 vs. Na^+/Na	67% after 200 cycles
$KMnFe(CN)_6$[27]	Cathode for SIBs	69	0.05C	3.3 vs. Na^+/Na	-
$KFeFe(CN)_6$[27]	Cathode for SIBs	100	0.05C	3.0 vs. Na^+/Na	-
$KCoFe(CN)_6$[27]	Cathode for SIBs	55	0.05C	3.25 vs. Na^+/Na	-
$KNiFe(CN)_6$[27]	Cathode for SIBs	52	0.05C	3.2 vs. Na^+/Na	-
$KCuFe(CN)_6$[27]	Cathode for SIBs	56	0.05C	3.2 vs. Na^+/Na	-
$KZnFe(CN)_6$[27]	Cathode for SIBs	35	0.05C	3.2 vs. Na^+/Na	-
$Na_2CoFe(CN)_6$[44]	Cathode for SIBs	150	10	3.42 vs. Na^+/Na	90 % after 200 cycles
$Na_2Zn_3[Fe(CN)_6]_2 \cdot xH_2O$[26]	Cathode for SIBs	56.4	10	3.3 vs. Na^+/Na	82.5% after 50 cycles
$Na_2Mn[Mn(CN)_6]_2 \cdot 2H_2O$[30]	Cathode for SIBs	209	0.2C	3.55 vs. Na^+/Na	78.3% after 100 cycles

Table 2. List of the performance characteristics of the representative PBAs for multivalent-ion (Mg/Al/Zn) batteries. ZIBs: zinc ion batteries. SCE: saturated calomel electrode.

Sample	application	Capacity (mAh g^{-1})	Current density (mA g^{-1})	Potential (V)	Cycling stability
$K_{0.86}Ni[Fe(CN)_6]_{0.954}(H_2O)_{0.766}$[112]	Organic electrolyte ZIBs	55.6	0.2C	1.19 vs. Zn^{2+}/Zn	80% after 6 cycles
$FeFe(CN)_6$[115]	Aqueous ZIBs	120	10	1.1 vs. Zn^{2+}/Zn	-
$KCuFe(CN)_6$[116]	Aqueous ZIBs	56	20	0.6 vs. Zn^{2+}/Zn	77% after 20 cycles
$Zn_3[Fe(CN)_6]2$[117]	Aqueous ZIBs	73.3	1 C	0.6 vs. Ag/AgCl	81% after 100 cycles
$KCuFe(CN)_6$[118]	Aqueous ZIB	50	60	0.8 vs. SHE	93% after 100 cycles
$KNiFe(CN)_6$[106]	Aqueous Mg-ion	52	0.2 C	0.6 vs. SHE	65% capacity

	batteries				retention after 2000 cycles
$K_{0.1}Cu[Fe(CN)_6]_{0.7}\cdot 3.6H_2O$[107]	Aqueous Mg-ion batteries	50	100	0.6 vs. Ag/AgCl	-
$KCuFe(CN)_6\cdot 8H_2O$[108]	Aqueous Al-ion batteries	62.9	50	0.54 vs. SCE	54.9% capacity retention after 1000 cycles
$KNiFe(CN)_6$[106]	Aqueous Ba-ion batteries	50	0.2 C	0.7 vs. SHE	93% capacity retention after 2000 cycles
$KNiFe(CN)_6$[106]	Aqueous Ca-ion batteries	50	0.2 C	0.6 vs. SHE	53% capacity retention after 2000 cycles

Dr. Wei-Jie Li received Master's degree (2012) from Central South University. She obtained her PhD degree from University of Wollongong, Australia. She is currently a research fellow at the institute for superconducting and electronic materials (ISEM), University of Wollongong (UOW). Her current research is focused on nanostructured and nanocomposite materials for energy storage (alkaline ion batteries and aqueous batteries) and conversion (photocatalyst, electrocatalyst)

Prof. Hua-Kun Liu is a distinguished Professor at Institute for Superconducting and Electronic Materials, University of Wollongong, Australia, and a Fellow of Australian Academy of Technological Science and Engineering. Her research interest in the Li/Na/K ion battereis, supercapacitor and catalysts.

This review provides a comprehensive overview of the latest research progress on the Prussian blue analogues, including the synthesis methods, structural and chemical properties of PBAs, various applications for these PBAs, and the effects of their structural and chemical properties on materials synthesis and applications. Finally, some personal viewpoints on the challenges and outlook for PBAs application are included.

Keyword: Prussian blue analogues, Chemical property, Structural property, Influence of properties on applications

Wei-Jie Li,* Chao Han, Shu-Lei Chou, Hua-Kun Liu*, Shi-Xue Dou

Chemical properties, structural properties, and applications of Prussian blue analogues

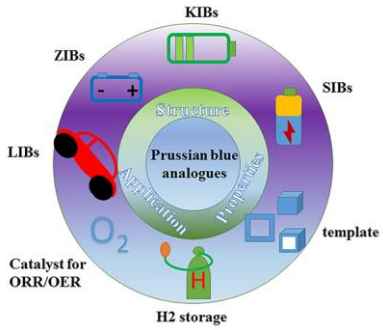

[1] Z. L. Wang, D. Xu, H. G. Wang, Z. Wu, X. B. Zhang, *ACS Nano* **2013**, *7*, 2422.
[2] H. X. Zhong, J. Wang, Y. W. Zhang, W. L. Xu, W. Xing, D. Xu, Y. F. Zhang, X. B. Zhang, *Angew. Chem. Int. Ed.* **2014**, *53*, 14235.
[3] D. L. Ma, Z. Y. Cao, H. G. Wang, X. L. Huang, L. M. Wang, X. B. Zhang, *Energy Environ. Sci.* **2012**, *5*, 8538.
[4] D. L. Ma, H. G. Wang, Y. Li, D. Xu, S. Yuan, X. L. Huang, X. B. Zhang, Y. Zhang, *Nano Energy* **2014**, *10*, 295.
[5] Y. H. Zhu, X. Yang, T. Sun, S. Wang, Y. L. Zhao, J. M. Yan, X. B. Zhang, *Electrochemical Energy Reviews* **2018**, *1*, 548.
[6] W. Li, S. L. Chou, J. Z. Wang, J. H. Kim, H. K. Liu, S. X. Dou, *Adv. Mater.* **2014**, *26*, 4037.
[7] W. J. Li, S. L. Chou, J. Z. Wang, H. K. Liu, S. X. Dou, *Chem. Commun.* **2015**, *51*, 3682.
[8] W. J. Li, S. L. Chou, J. Z. Wang, Y. M. Kang, J. L. Wang, Y. Liu, Q. F. Gu, H. K. Liu, S. X. Dou, *Chem. Mater.* **2015**, *27*, 1997.
[9] W. J. Li, Q. R. Yang, S. L. Chou, J. Z. Wang, H. K. Liu, *J Power Sources* **2015**, *294*, 627.
[10] W. J. Li, C. Han, S. L. Chou, J. Z. Wang, Z. Li, Y. M. Kang, H. K. Liu, S. X. Dou, *Chem. Eur. J.* **2016**, *22*, 590.
[11] Y. Wei, J. Xiong, W. Li, R. H. Kollarigowda, G. Cheng, *Inorg. Chem. Front.* **2018**, *5*, 2709.
[12] Y. H. Zhu, X. Yang, D. Bao, X. F. Bie, T. Sun, S. Wang, Y. S. Jiang, X. B. Zhang, J. M. Yan, Q. Jiang, *Joule* **2018**, *2*, 736.
[13] Y. H. Zhu, Y. B. Yin, X. Yang, T. Sun, S. Wang, Y.S. Jiang, J. M. Yan, X. B. Zhang, *Angew. Chem. Int. Ed.* **2017**, *56*, 7881.
[14] Y. H. Zhu, S. Yuan, D. Bao, Y. B. Yin, H. X. Zhong, X. B. Zhang, J. M. Yan, Q. Jiang, *Adv. Mater.* **2017**, *29*, 1603719.

[15] W. J. Li, S. L. Chou, J. Z. Wang, H. K. Liu, S. X. Dou, *J. Mater. Chem. A* **2016**, *4*, 505.
[16] Z. Jian, V. Raju, Z. Li, Z. Xing, Y. S. Hu, X. Ji, *Adv. Funct. Mater.* **2015**, *25*, 5778.
[17] Y. Sun, S. Guo, H. Zhou, *Energy Environ. Sci.* **2018,** DOI: 10.1039/c8ee01006d.
[18] S. Ferlay, T. Mallah, R. Ouahès, P. Veillet, M. Verdaguer, *Nature* **1995**, *378*, 701.
[19] J. Peng, J. Wang, H. Yi, W. Hu, Y. Yu, J. Yin, Y. Shen, Y. Liu, J. Luo, Y. Xu, P. Wei, Y. Li, Y. Jin, Y. Ding, L. Miao, J. Jiang, J. Han, Y. Huang, *Adv. Energy Mater.***2018***, 8,* 1702856.
[20] M. Zhou, L. Zhu, Y. Cao, R. Zhao, J. Qian, X. Ai, H. Yang, *RSC Adv.* **2012**, *2*, 5495.
[21] J. Chen, K. Huang, S. Liu, *Electrochem. Commun.* **2008**, *10*, 1851.
[22] C. D. Wessells, R. A. Huggins, Y. Cui, *Nat. Commun.* **2011**, *2*, 550.
[23] C. D. Wessells, S. V. Peddada, R. A. Huggins, Y. Cui, *Nano Lett.* **2011**, *11*, 5421.
[24] M. Zhou, J. Qian, X. Ai, H. Yang, *Adv. Mater.* **2011**, *23*, 4913.
[25] D. Asakura, M. Okubo, Y. Mizuno, T. Kudo, H. Zhou, K. Ikedo, T. Mizokawa, A. Okazawa, N. Kojima, *J.Phys.Chem. C* **2012**, *116*, 8364.
[26] H. Lee, Y. I. Kim, J. K. Park, J. W. Choi, *Chem. Commun.* **2012**, *48*, 8416.
[27] Y. Lu, L. Wang, J. Cheng, J. B. Goodenough, *Chem. Commun.* **2012**, *48*, 6544.
[28] C. D. Wessells, S. V. Peddada, M. T. McDowell, R. A. Huggins, Y. Cui, *J. Electrochem. Soc.* **2012**, *159*, A98.
[29] L. Wang, Y. Lu, J. Liu, M. Xu, J. Cheng, D. Zhang, J. B. Goodenough, *Angew. Chem. Int. Ed.* **2013**, *52*, 1964.
[30] H. W. Lee, R. Y. Wang, M. Pasta, S. Woo Lee, N. Liu, Y. Cui, *Nat.Commun.* **2014**, *5*, 5280.
[31] M. Okubo, C. H. Li, D. R. Talham, *Chem. Commun.* **2014**, *50*, 1353.
[32] D. Yang, J. Xu, X. Z. Liao, Y. S. He, H. Liu, Z. F. Ma, *Chem. Commun.* **2014**, *50*, 13377.
[33] Y. You, X. L. Wu, Y. X. Yin, Y. G. Guo, *Energy Environ. Sci.* **2014**, *7*, 1643.
[34] Y. Yue, A. J. Binder, B. Guo, Z. Zhang, Z. A. Qiao, C. Tian, S. Dai, *Angew. Chem. Int. Ed.* **2014**, *53*, 3134.
[35] K. Ono, M. Ishizaki, S. Soma, K. Kanaizuka, T. Togashi, M. Kurihara, *RSC Adv.* **2015**, *5*, 96297.
[36] J. Song, L. Wang, Y. Lu, J. Liu, B. Guo, P. Xiao, J. J. Lee, X. Q. Yang, G. Henkelman, J. B. Goodenough, *J. Am. Chem. Soc.* **2015**, *137*, 2658.
[37] L. Wang, J. Song, R. Qiao, L. A. Wray, M. A. Hossain, Y. D. Chuang, W. Yang, Y. Lu, D. Evans, J. J. Lee, S. Vail, X. Zhao, M. Nishijima, S. Kakimoto, J. B. Goodenough, *J. Am. Chem. Soc.* **2015**, *137*, 2548.
[38] D. Yang, J. Xu, X. Z. Liao, H. Wang, Y. S. He, Z. F. Ma, *Chem. Commun.* **2015**, *51*, 8181.
[39] Z. Ji, B. Han, H. Liang, C. Zhou, Q. Gao, K. Xia, J. Wu, *ACS Appl. Mater.Interfaces* **2016**, *8*, 33619.
[40] Y. Jiang, S. Yu, B. Wang, Y. Li, W. Sun, Y. Lu, M. Yan, B. Song, S. Dou, *Adv. Funct. Mater.* **2016,** *26*, 5315.
[41] J. H. Lee, G. Ali, D. H. Kim, K. Y. Chung, *Adv. Energy Mater.* **2016**, 1601491.
[42] Y. Tang, W. Zhang, L. Xue, X. Ding, T. Wang, X. Liu, J. Liu, X. Li, Y. Huang, *J. Mater. Chem. A* **2016**, *4*, 6036.
[43] X. Wu, M. Shao, C. Wu, J. Qian, Y. Cao, X. Ai, H. Yang, *ACS Appl. Mater. Interfaces* **2016**, *8*, 23706.
[44] X. Wu, C. Wu, C. Wei, L. Hu, J. Qian, Y. Cao, X. Ai, J. Wang, H. Yang, *ACS Appl. Mater. Interfaces* **2016**, *8*, 5393.
[45] Y. You, H. R. Yao, S. Xin, Y. X. Yin, T. T. Zuo, C. P. Yang, Y. G. Guo, Y. Cui, L. J. Wan, J. B. Goodenough, *Adv. Mater.* **2016**, *28*, 7243.

[46] X. Bie, K. Kubota, T. Hosaka, K. Chihara, S. Komaba, *J. Mater. Chem. A* **2017**, *5*, 4325.
[47] F. Bu, X. Feng, T. Jiang, I. Shakir, Y. Xu, *Chem. Eur. J.* **2017**, *23*, 8358.
[48] G. He, L. F. Nazar, *ACS Energy Lett.* **2017**, *2*, 1122.
[49] Y. Huang, M. Xie, J. Zhang, Z. Wang, Y. Jiang, G. Xiao, S. Li, L. Li, F. Wu, R. Chen, *Nano Energy* **2017**, *39*, 273.
[50] Y. Liu, D. He, R. Han, G. Wei, Y. Qiao, *Chem. Commun.* **2017**, *53*, 5569.
[51] Y. Liu, G. Wei, M. Ma, Y. Qiao, *Chem. Eur. J.* **2017**, *23*, 15991.
[52] J. Luo, S. Sun, J. Peng, B. Liu, Y. Huang, K. Wang, Q. Zhang, Y. Li, Y. Jin, Y. Liu, Y. Qiu, Q. Li, J. Han, Y. Huang, *ACS Appl. Mater.Interfaces* **2017**, *9*, 25317.
[53] W. Ren, M. Qin, Z. Zhu, M. Yan, Q. Li, L. Zhang, D. Liu, L. Mai, *Nano Lett.* **2017**, *17*, 4713.
[54] H. Wang, L. Wang, S. Chen, G. Li, J. Quan, E. Xu, L. Song, Y. Jiang, *J. Mater. Chem. A* **2017**, *5*, 3569.
[55] L. Xue, Y. Li, H. Gao, W. Zhou, X. Lü, W. Kaveevivitchai, A. Manthiram, J. B. Goodenough, *J. Am. Chem. Soc.* **2017**, *139*, 2164.
[56] X. Bie, K. Kubota, T. Hosaka, K. Chihara, S. Komaba, *J. Power Sources* **2018**, *378*, 322.
[57] Y. Huang, M. Xie, Z. Wang, Y. Jiang, Y. Yao, S. Li, Z. Li, L. Li, F. Wu, R. Chen, *Small* **2018**, *14*, 1801246.
[58] M. Oliver-Tolentino, M. González M, H. Osiry, G. Ramos-Sánchez, I. González, *Dalton Trans.* **2018**, *47*, 16492.
[59] W. Li, C. Han, Q. Xia, K. Zhang, S. Chou, Y. M. Kang, J. Wang, H. K. Liu, S. X. Dou, *Small Methods* **2018**, *2*, 1700346.
[60] J. Peng, J. Wang, H. Yi, W. Hu, Y. Yu, J. Yin, Y. Shen, Y. Liu, J. Luo, Y. Xu, P. Wei, Y. Li, Y. Jin, Y. Ding, L. Miao, J. Jiang, J. Han, Y. Huang, *Adv. Energy Mater.* **2018**, *8*, 1702856.
[61] X. Tang, H. Liu, D. Su, P. H. L. Notten, G. Wang, *Nano Research* **2018**, *11*, 3979.
[62] H. Yao, F. Zhang, G. Zhang, Y. Yang, *Electrochim. Acta* **2019**, *294*, 286.
[63] W. J. Li, S. L. Chou, J. Z. Wang, J. L. Wang, Q. F. Gu, H. K. Liu, S. X. Dou, *Nano Energy* **2015**, *13*, 200.
[64] S. S. Kaye, J. R. Long, *Catal. Today* **2007**, *120*, 311.
[65] S. S. Kaye, J. R. Long, *J. Am. Chem. Soc.* **2005**, *127*, 6506.
[66] K. W. Chapman, P. D. Southon, C. L. Weeks, C. J. Kepert, *Chem. Commun.* **2005**, 3322.
[67] A. Indra, U. Paik, T. Song, *Angew. Chem. Int. Ed.*, **2017**, *56*, 1.
[68] S. Pintado, S. Goberna-Ferrón, E. C. Escudero-Adán, J. R. Galán-Mascarós, *J. Am. Chem. Soc.* **2013**, *135*, 13270.
[69] M. B. Zakaria, V. Malgras, T. Takei, C. Li, Y. Yamauchi, *Chem. Commun.* **2015**, *51*, 16409.
[70] B. K. Barman, K. K. Nanda, *Green Chem.* **2016**, *18*, 427.
[71] L. Du, C. Du, G. Chen, F. Kong, G. Yin, Y. Wang, *ACS Appl. Mater. Interfaces* **2016**, *8*, 15250.
[72] Y. Liu, H. Wang, D. Lin, J. Zhao, C. Liu, J. Xie, Y. Cui, *Nano Research* **2017**, *10*, 1213.
[73] W. Ahn, M. G. Park, D. U. Lee, M. H. Seo, G. Jiang, Z. P. Cano, F. M. Hassan, Z. Chen, *Adv. Funct. Mater.* **2018**, *28*, 1802129.
[74] X. Su, Y. Wang, J. Zhou, S. Gu, J. Li, S. Zhang, *J. Am. Chem. Soc.* **2018,** *140,* 36.
[75] S. S. Kumar, J. Joseph, K. L. Phani, *Chem. Mater.* **2007**, *19*, 4722.
[76] M. Pasta, R. Y. Wang, R. Ruffo, R. Qiao, H. W. Lee, B. Shyam, M. Guo, Y. Wang, L. A. Wray, W. Yang, M. F. Toney, Y. Cui, *J. Mater. Chem. A* **2016**, *4*, 4211.

[77] K. Lu, B. Song, J. Zhang, H. Ma, *J. Power Sources* **2016**, *321*, 257.
[78] L. Hu, P. Zhang, Q. W. Chen, N. Yan, J.-y. Mei, *Dalton Trans.* **2011**, *40*, 5557.
[79] M. Hu, J. S. Jiang, R. P. Ji, Y. Zeng, *CrystEngComm* **2009**, *11*, 2257.
[80] S. Kang, S. Im, Y. Jeon, *Bull. Korean Chem. Soc.* **2015**, *36*, 2387.
[81] M. Cao, X. Wu, X. He, C. Hu, *Chem. Commun.* **2005**, 2241.
[82] D. N. Vernon, *J. Electrochem. Soc.*, *125*, 886.
[83] F. Qu, A. Shi, M. Yang, J. Jiang, G. Shen, R. Yu, *Analytica Chimica Acta* **2007**, *605*, 28.
[84] P. Zhou, D. Xue, H. Luo, X. Chen, *Nano Lett.* **2002**, *2*, 845.
[85] A. Johansson, E. Widenkvist, J. Lu, M. Boman, U. Jansson, *Nano Lett.* **2005**, *5*, 1603.
[86] C. Zhang, Y. Xu, M. Zhou, L. Liang, H. Dong, M. Wu, Y. Yang, Y. Lei, *Adv. Funct. Mater.* **2017**, *27*, 1604307.
[87] L. Zhang, H. B. Wu, X. W. Lou, *J. Am. Chem. Soc.* **2013**, *135*, 10664.
[88] L. Han, X. Y. Yu, X. W. Lou, *Adv. Mater.* **2016**, *28*, 4601.
[89] M. Hu, S. Furukawa, R. Ohtani, H. Sukegawa, Y. Nemoto, J. Reboul, S. Kitagawa, Y. Yamauchi, *Angew. Chem. Int. Ed.* **2012**, *51*, 984.
[90] X. Jia, X. Cai, Y. Chen, S. Wang, H. Xu, K. Zhang, M. Ma, H. Wu, J. Shi, H. Chen, *ACS Appl. Mater. Interfaces* **2015**, *7*, 4579.
[91] M. Hu, A. A. Belik, M. Imura, K. Mibu, Y. Tsujimoto, Y. Yamauchi, *Chem. Mater.* **2012**, *24*, 2698.
[92] W. Chen, K. Zeng, H. Liu, J. Ouyang, L. Wang, Y. Liu, H. Wang, L. Deng, Y.-N. Liu, *Adv. Funct. Mater.* **2017**, *27*, 1605795.
[93] N. L. Torad, M. Hu, M. Imura, M. Naito, Y. Yamauchi, *J. Mater. Chem.* **2012**, *22*, 18261.
[94] G. Yilmaz, C. F. Tan, M. Hong, G. W. Ho, *Adv. Funct. Mater.* **2018**, *28*, 1704177.
[95] Y. Liu, J. Goebl, Y. Yin, *Chem. Soc. Rev.* **2013**, *42*, 2610.
[96] O. N. Risset, E. S. Knowles, S. Ma, M. W. Meisel, D. R. Talham, *Chem. Mater.* **2013**, *25*, 42.
[97] Y. Fang, X. Y. Yu, X. W. Lou, *Adv. Mater.* **2018**, *30*, 1706668.
[98] X.-Y. Yu, L. Yu, H. B. Wu, X. W. Lou, *Angew. Chem. Int. Ed.* **2015**, *54*, 5331.
[99] L. Xue, H. Gao, Y. Li, J. B. Goodenough, *J. Am. Chem. Soc.* **2018**.
[100] D. R. Shi, J. Fu, Z. Shadike, M. H. Cao, W. W. Wang, Z. W. Fu, *ACS Omega* **2018**, *3*, 7648.
[101] J. Qian, C. Wu, Y. Cao, Z. Ma, Y. Huang, X. Ai, H. Yang, *Adv. Energy Mater.* **2018**, *8*, 1702619.
[102] W. J. Li, C. Han, W. Wang, F. Gebert, S. L. Chou, H. K. Liu, X. Zhang, S. X. Dou, *Adv. Energy Mater.* **2017**, *7*, 1700274.
[103] L. Shen, Z. Wang, L. Chen, *Chem. Eur. J.* **2014**, *20*, 12559.
[104] L. Deng, Z. Yang, L. Tan, L. Zeng, Y. Zhu, L. Guo, *Adv. Mater.* **2018**, *30*, 1802510.
[105] P. Nie, L. Shen, H. Luo, B. Ding, G. Xu, J. Wang, X. Zhang, *J. Mater. Chem. A* **2014**, *2*, 5852.
[106] R. Y. Wang, C. D. Wessells, R. A. Huggins, Y. Cui, *Nano Lett.* **2013**, *13*, 5748.
[107] Y. Mizuno, M. Okubo, E. Hosono, T. Kudo, K. Oh-ishi, A. Okazawa, N. Kojima, R. Kurono, S. I. Nishimura, A. Yamada, *J. Mater. Chem. A* **2013**, *1*, 13055.
[108] S. Liu, G. L. Pan, G. R. Li, X. P. Gao, *J. Mater. Chem. A* **2015**, *3*, 959.
[109] L. Han, P. Tang, Á. Reyes-Carmona, B. Rodríguez-García, M. Torréns, J. R. Morante, J. Arbiol, J. R. Galan-Mascaros, *J. Am. Chem. Soc.* **2016**, *138*, 16037.
[110] X. Wang, L. Yu, B. Y. Guan, S. Song, X. W. Lou, *Adv. Mater.* **2018**, *30*, 1801211.
[111] C. M. Kareis, S. H. Lapidus, J. H. Her, P. W. Stephens, J. S. Miller, *J. Am. Chem. Soc.* **2012**, *134*, 2246.

[112] M. S. Chae, J. W. Heo, H. H. Kwak, H. Lee, S.-T. Hong, *J. Power Sources* **2017**, *337*, 204.
[113] Z. Shadike, D. R. Shi, W. Tian, M. H. Cao, S. F. Yang, J. Chen, Z. W. Fu, *J. Mater. Chem. A* **2017**, *5*, 6393.
[114] M. Morant-Giner, R. Sanchis-Gual, J. Romero, A. Alberola, L. García-Cruz, S. Agouram, M. Galbiati, N. M. Padial, J. C. Waerenborgh, C. Martí-Gastaldo, S. Tatay, A. Forment-Aliaga, E. Coronado, *Adv. Funct. Mater.* **2018**, *28*, 1706125.
[115] Z. Liu, G. Pulletikurthi, F. Endres, *ACS Appl. Mater. Interfaces* **2016**, *8*, 12158.
[116] Z. Jia, B. Wang, Y. Wang, *Mater. Chem. Phy.* **2015**, *149-150*, 601.
[117] L. Zhang, L. Chen, X. Zhou, Z. Liu, *Adv. Energy Mater.* **2015**, *5*, 1400930.
[118] R. Trócoli, F. La Mantia, *ChemSusChem* **2015**, *8*, 481.